Remote Sensing of Environment 312 (2024) 114343

Contents lists available at ScienceDirect

Remote Sensing of Environment

journal homepage: www.elsevier.com/locate/rse

A global urban heat island intensity dataset: Generation, comparison, and analysis

Qiquan Yang [a,b,c], Yi Xu [a,*], TC Chakraborty [d], Meng Du [e], Ting Hu [e], Ling Zhang [f], Yue Liu [g], Rui Yao [h], Jie Yang [h], Shurui Chen [b], Changjiang Xiao [b,c], Renrui Liu [a], Mingjie Zhang [a], Rui Chen [a]

[a] State Key Laboratory of Lunar and Planetary Sciences, Macau University of Science and Technology, Macau, China
[b] College of Surveying & Geo-Informatics, Tongji University, Shanghai 200092, China
[c] The Shanghai Key Laboratory of Space Mapping and Remote Sensing for Planetary Exploration, Tongji University, Shanghai 200092, China
[d] Atmospheric, Climate, and Earth Sciences Division, Pacific Northwest National Laboratory, Richland, WA, USA
[e] School of Remote Sensing and Geomatics Engineering, Nanjing University of Information Science and Technology, Nanjing 210044, China
[f] School of Earth Science and Geological Engineering, Sun Yat-sen University, Guangzhou 510275, China
[g] Guangzhou Institute of Geography, Guangdong Academy of Sciences, Guangzhou 510070, China
[h] School of Remote Sensing and Information Engineering, Wuhan University, Wuhan 430079, China

ARTICLE INFO

Editor: Jing M. Chen

Keywords:
Urban thermal environment
Urban warming trend
Rural definition
Estimation method
Spatiotemporal variation

ABSTRACT

The urban heat island (UHI) effect, a phenomenon of local warming over urban areas, is the most well-known impact of urbanization on climate. Globally consistent estimates of the UHI intensity (UHII) are crucial for examining this phenomenon across time and space. However, publicly available UHII datasets are limited and have several constraints: (1) they are for clear-sky surface UHII, not all-sky surface UHII and canopy (air temperature) UHII; (2) the estimation methods often neglect anthropogenic disturbance, introducing uncertainties in the estimated UHII. To address these issues, this study proposes a new dynamic equal-area (DEA) method that can minimize the influence of various confounding factors on UHII estimates through a dynamic cyclic process. Utilizing the DEA method and leveraging various gridded temperature data, we develop a global-scale (>10,000 cities), long-term (over 20 years by month), and multi-faceted (clear-sky surface, all-sky surface, and canopy) UHII dataset. Based on these estimates, we provide a comprehensive analysis of the UHII and its trends in global cities. The UHII is found to be greater than zero in >80% of cities, with global annual average magnitudes around 1.0 °C (day) and 0.8 °C (night) for surface UHII, and close to 0.5 °C for canopy UHII. Furthermore, an interannual upward trend in UHII is observed in >60% of cities, with global annual average trends exceeding 0.1 °C/decade (day) and over 0.06 °C/decade (night) for surface UHII, and slightly surpassing 0.03 °C/decade for canopy UHII. Notably, there exists a positive correlation between the magnitude and trend of UHII, suggesting that cities with stronger UHII tend to experience faster growth in UHII. Additionally, discrepancies in UHII are found between different temperature data, stemming not only from distinctions in data types (surface or air temperature) but also from differences in data acquisition times (Terra or Aqua), weather conditions (clear-sky or all-sky), and processing methodologies (with or without gap filling). Overall, our proposed method, dataset, and analysis results have the potential to provide valuable insights for future urban climate studies. The UHII dataset is publicly available at https://doi.org/10.6084/m9.figshare.24821538.

1. Introduction

Urban heat island (UHI) effect refers to the phenomenon where the temperature in urban areas is higher than that in the surrounding rural areas (Rizwan et al., 2008). This phenomenon can have various adverse impacts, including increased heat stress and health risks for residents, rising energy demands and economic burdens, deterioration of air quality, increased pressure on water resources, and the potential exacerbation of social inequalities and vulnerabilities within urban areas (Chakraborty et al., 2023; Hsu et al., 2021; Li et al., 2018a; Li et al.,

* Corresponding author.
E-mail address: yixu@must.edu.mo (Y. Xu).

https://doi.org/10.1016/j.rse.2024.114343
Received 29 December 2023; Received in revised form 26 June 2024; Accepted 26 July 2024
Available online 30 July 2024

2019d; Zhou et al., 2018). The UHI intensity (UHII) is the main way to quantify the strength of the UHI signal, reflecting the average temperature difference between the urban area and its background reference area (BRA). Several studies have extensively analyzed the UHII at regional or global scales, with a primary focus on its spatiotemporal variations, driving factors, and potential impacts (Cai et al., 2023; Chen et al., 2023; Clinton and Gong, 2013; Du et al., 2016; Du et al., 2023; Gui et al., 2019; Li et al., 2019a; Li and Chen, 2023; Liu et al., 2021; Manoli et al., 2020; Peng et al., 2012; Ren et al., 2023; Shao et al., 2023; Yang and Zhao, 2023; Yao et al., 2018a; Yao et al., 2019; Yao et al., 2017; Zhao et al., 2014; Zhou et al., 2017; Zhou et al., 2014).

Accurate estimation of the UHII using a consistent method is a prerequisite for further analysis of this local urban climate signal across regions. Several global and regional datasets have been generated for this purpose. For instance, a global dataset of summertime surface UHII during 2013 was produced by using the Moderate Resolution Imaging Spectroradiometer (MODIS) land surface temperature (LST) products (Center for International Earth Science Information Network - CIESIN - Columbia University, 2016). This global-scale dataset has been used for examining the spatial patterns of surface UHI effect and exploring its relationship with demographic factors and prevailing climatic conditions (Manoli et al., 2019). Based on the proposed simplified urban-extent (SUE) algorithm, Chakraborty and Lee (2019) produced a multi-year monthly surface UHII dataset encompassing almost 10,000 cities worldwide. They then built upon this data to analyze the spatial and temporal patterns in surface UHI effect, exploring their relationship with vegetation index. Subsequently, Chakraborty et al. (2020) modified the SUE algorithm and leveraged it to create a spatially explicit surface UHII database exclusively dedicated to the United States. This data was used to analyze the spatiotemporal variability of heat islands in the urbanized areas and combined with census data to reveal the inequity in heat exposure across different ethnic and income groups (Hsu et al., 2021). Niu et al. (2021) utilized the MODIS 8-day composite LST product to create a surface UHII dataset covering 286 Chinese cities from 2001 to 2018, and further examined the spatial patterns and inter-annual trends in surface UHII across China. Besides MODIS, Devereux and Caccetta (2019) retrieved LST of Australian major cities by using the Landsat 8 thermal infrared images, and further calculated the urban-rural LST difference to form a surface UHII dataset. Chakraborty et al. (2021a) developed a global ensemble surface UHII dataset using the SUE algorithm based on Landsat LST and multiple surface emissivity models. The UHII datasets generated by current studies have played a crucial role in advancing research within the academic community. However, the existing UHII datasets concentrate on utilizing remotely sensed LST data for deriving surface UHII. This gives rise to two challenges: (1) the accuracy of the estimated surface UHII is impacted by the occurrence of missing data in the LST observations, which can only be acquired under clear-sky conditions (Liao et al., 2022); (2) the surface UHII derived from LST may not be representative of the canopy UHII across scales, the latter being more closely associated with human perception of heat and requiring air temperature data (Du et al., 2023; Venter et al., 2021). In recent years, numerous data fusion techniques have emerged that can effectively interpolate missing data to seamlessly generate LST data under all weather conditions (Mo et al., 2021). Moreover, machine learning methods have demonstrated efficacy in obtaining high-accuracy surface air temperature (SAT) by synthesizing sparse in-situ observations with a diverse set of surface attributes (Chen et al., 2022; Yao et al., 2023). At present, several global-scale spatially seamless LST and SAT datasets have been made publicly accessible (Hong et al., 2022; Jia et al., 2023; Yao et al., 2023; Yu et al., 2022; Zhang et al., 2022a; Zhang et al., 2022b). These datasets play a vital role as a complement to existing clear-sky LST products (e.g., MODIS), offering new avenues for studying and addressing challenges associated with urban climate impacts.

Currently available UHII datasets exhibit variations in their estimation methods, primarily attributed to disparities in the selection of BRAs. For instance, the global surface UHI dataset released by CIESIN applied a distance-based method, which defined the BRA as a constant 10 km buffer area around the central urban area for all cities (Center for International Earth Science Information Network - CIESIN - Columbia University, 2016). The applicability of such distance-based method is limited by the challenge of applying a single fixed buffer to cities of varying sizes, particularly in the context of large-scale studies (Lai et al., 2018; Yang et al., 2023b). The surface UHII dataset produced by Chakraborty and Lee (2019) was generated using a SUE algorithm, which defined the BRA as the non-built-up pixels within urban agglomerations. The SUE method avoids buffer selection but faces challenges from anthropogenic disturbance, primarily due to the proximity of the selected BRA to urban areas (Li et al., 2022; Yang et al., 2023b). Many studies have used area-based methods to select the BRA, most typically defining the BRA as the equal-area buffer surrounding the central urban area (Chakraborty et al., 2021b; Peng et al., 2012; Yang et al., 2017; Zhou et al., 2014). Such equal-area methods take the size of the urban area into account when selecting the BRA, making them suitable for multi-city UHI analysis (Li et al., 2022; Yang et al., 2023b). However, traditional equal-area methods also encounter anthropogenic disturbance and may consequently underestimate the UHII (Yang et al., 2023b). Recently, Li et al. (2022) modified traditional equal-area methods by excluding areas within the BRA with nighttime light intensity (NLI) higher than the median value. This modified equal-area method can mitigate the influence of anthropogenic disturbance on UHII estimates, but further optimization is needed due to the following reasons: (1) potential incomplete exclusion may arise when using the median NLI in the BRA as a threshold, particularly in cities with relatively high NLI in urban surroundings; (2) while the NTL can indicate human activities, it may overlook man-made disturbance in areas with low illumination or where lighting isn't necessary (Levin et al., 2020; Zhao et al., 2019). As an alternative, a number of studies have used the impervious surface fraction (ISF) as a criterion for filtering the BRA (Imhoff et al., 2010; Yang and Zhao, 2023; Yang et al., 2023a; Yao et al., 2018b). For example, Yang et al. (2023a) and Yao et al. (2018b) removed all areas with an ISF exceeding 5% from the BRA to ensure that it closely reflects the natural state of the ground. However, these studies did not dynamically adjust for the size of the BRA when removing areas with high ISF values, resulting in a significant reduction or complete absence of available BRA pixels (Liu et al., 2023; Yang et al., 2023a). In addition to anthropogenic disturbance, the selection of the BRA also requires the removal of other confounding factors, such as water bodies and topographic relief (Yang et al., 2023b). Therefore, developing a new method suitable for large-scale studies, capable of effectively mitigating the influence of various confounding factors, is essential for establishing a reliable and globally consistent UHII dataset.

To address the above problems, we have made efforts in this study from the following aspects. First, drawing on the strengths of existing area-based methods, we introduce a new dynamic equal-area (DEA) method for estimating UHI. This method can minimize the influence of various confounding factors through a dynamic cyclic process, better emphasizing the impact of urbanization on local temperature. Second, utilizing the DEA method and leveraging various gridded temperature data, we develop a global-scale (covering >10,000 cities), long-term (over 20 years by month), and multi-faceted (clear-sky surface, all-sky surface, and canopy) UHII dataset. This UHII dataset fills the gap of publicly available global-scale datasets of all-sky surface or canopy UHII. Third, based on our UHII dataset, we make a comprehensive analysis of the magnitude and trend of UHII, and perform a systematic comparison of UHII estimates derived from different temperature data. These analyses contribute to obtaining a more objective and comprehensive assessment of the spatiotemporal patterns and changing tendencies of the UHI effect. Overall, our proposed DEA method, published UHII dataset, and analysis results are anticipated to provide valuable reference for future research on urban thermal environments.

2. Data

2.1. Land cover data

The MODIS land cover type product (MCD12Q1) can provide annual global-scale extent of "urban and built-up". Based on previous studies (Peng et al., 2012; Si et al., 2022; Zhou et al., 2017), we employed the city clustering algorithm (CCA) to aggregate "urban and built-up" pixels, categorizing pixels close to each other (within 2 km) as part of the same urban cluster. We processed all MCD12Q1 data for the period 2001–2021 as described above and derived global urban clusters for different years. To maintain consistency in urban clusters over the years, we standardized urban clusters in previous years by referencing those of the latest year (2021). Specifically, urban clusters that were treated as separate entities in earlier years but were identified as the same one in 2021 were further aggregated into a single urban cluster. This procedure facilitates comparative analysis of results across various years. Subsequently, we identified urban clusters that consistently exceeded 9 km^2 for all years (2001−2021), totaling 10,196 globally. These urban clusters (or called cities) are distributed across various climate zones, encompassing tropical (1480), arid (2193), temperate (3708), cold (2806), and polar (9) zones (Fig. 1). In addition, we identified pixels labelled as "water" or "permanent wetland" in MCD12Q1 for each year to prepare for removing the influence of water bodies on UHII estimates (Chakraborty and Lee, 2019; Lai et al., 2018).

2.2. Temperature data

The MODIS LST products were used to derive UHII under clear-sky conditions. Four MODIS LST products have been frequently used in UHI-related studies (Zhou et al., 2018): MOD11A1 (Mod1), MOD11A2 (Mod2), MYD11A1 (Myd1), and MYD11A2 (Myd2). Among these, Mod1 and Mod2 originate from the Terra satellite (with transit times at ~10:30 and ~ 22:30 local time), while Myd1 and Myd2 are derived from the Aqua satellite (with transit times at ~13:30 and ~ 1:30 local time). Mod1 and Myd1 are daily products, while Mod2 and Myd2 are 8-day composite products.

To reduce the bias in UHII estimation caused by missing LST data, recent studies have favored the use of gap-filled seamless LST data (Yang and Zhao, 2023; Yang et al., 2023b). Hence, this study incorporated two recently introduced seamless LST products, namely SMod2 and SMyd1. Among them, SMod2 was developed by Yao et al. (2023) through the interpolation of the original Mod2 product, while SMyd1 was produced by Zhang et al. (2022b) through the interpolation of the original Myd1 product. It should be noted that SMod2 and SMyd1 were interpolated without accounting for weather conditions, thereby still representing the LST under clear-sky conditions (Yao et al., 2023; Zhang et al., 2022b). Given the difference between clear-sky and all-sky LSTs, we incorporated the spatial-seamless all-sky LST data, denoted as AMod2, generated by Yao et al. (2023) using the original Mod2 product. The accuracies of these seamless LST datasets, namely SMod2, SMyd1, and AMod2, have been extensively evaluated and they have been effectively employed in various recent studies (Liu et al., 2023; Yang and Zhao, 2023; Yang et al., 2023b; Yuan et al., 2023).

Besides the above LST datasets, we also incorporated the gridded SAT dataset produced by Yao et al. (2023) for the assessment of canopy UHII. The gridded SAT dataset was generated from the seamless Mod2 LST observations, the in-situ air temperature measurements, and the Cubist machine learning algorithm (Yao et al., 2023). Validation results showed good accuracy of the reconstructed gridded SAT data, with the global mean absolute errors <1 °C (Yao et al., 2023). It can provide both the maximum and minimum temperatures of a day, corresponding to the daytime and nighttime observations of the LST data, respectively.

These temperature datasets exhibit a spatial resolution of 1 km, and apart from the original MODIS LST products, they are accessible only up to the year 2020. These temperature datasets underwent separate monthly averaging, followed by subsequent seasonal and annual averaging. In the Northern Hemisphere (Southern Hemisphere), the months corresponding to spring are March–May (September–November), to summer are June–August (December–February), to Autumn are September–November (March–May), and to winter are December–February (June–August).

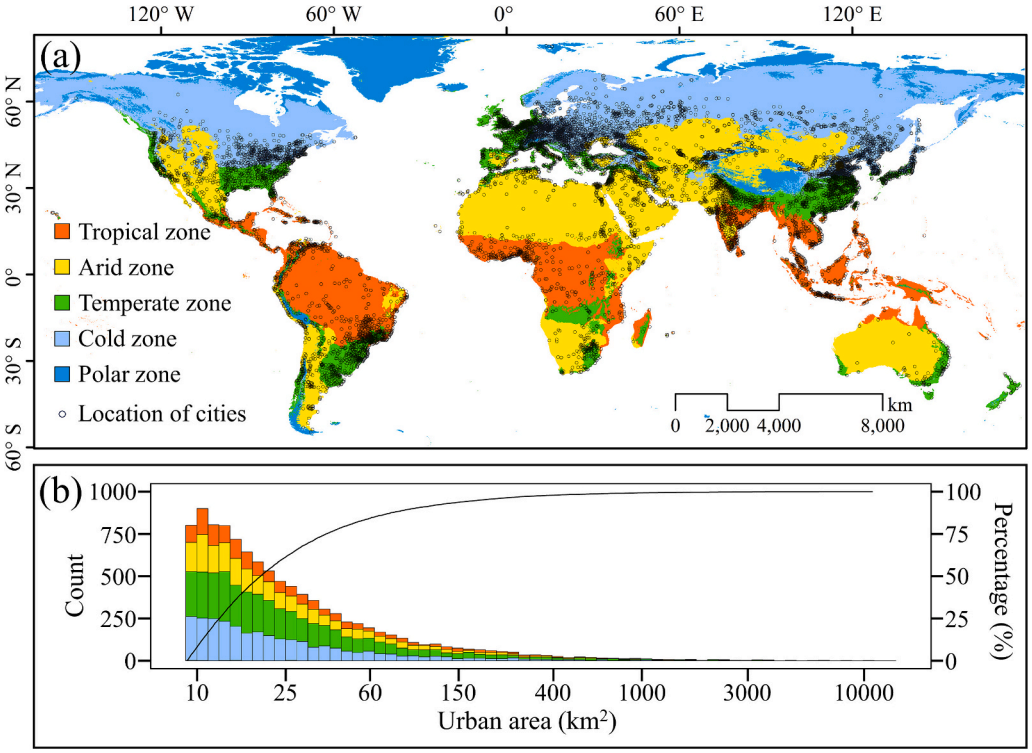

Fig. 1. Spatial distributions of global cities. (a) Location and climate type of the 10,196 selected cities. (b) Number and percentage of cities categorized by their sizes.

2.3. Auxiliary data

Nighttime light intensity (NLI): The intensity of nighttime lights serves as an indicator of human activity and can be used for identifying areas within the BRA affected by anthropogenic disturbance. This study utilized the global NPP-VIIRS-like NLI data developed by Chen et al. (2021). This dataset boasts an extended timescale in comparison to the original NPP-VIIRS NTL data, demonstrating good quality in both spatial pattern and temporal consistency (Chen et al., 2021). The NPP-VIIRS-like NTL data products used in this study cover the period 2001–2021.

Impervious surface fraction (ISF): In addition to addressing NLI, this study further mitigated the influence of anthropogenic disturbance by using the global impervious surface area (GISA) data developed by Huang et al. (2022). This data provides the spatial distribution of impervious surface across the globe at a 30-m resolution. The GISA has been recently updated to 2021, and we utilized the annual data spanning the period from 2001 to 2021. Using this data, we computed the proportion of impervious surface within each temperature pixel extent, resulting in global ISF data for each year spanning from 2001 to 2021.

Digital elevation model (DEM): The Global 30 Arc-Second Elevation (GTOPO30) data, developed by United States Geological Survey (USGS), can provide the elevation information of Earth's terrain at a spatial resolution of approximately 1 km. It was used for reducing the influence of topographic relief on UHII estimates.

Climate classification map: The Köppen-Geiger Climate Classification global map, generated by Beck et al. (2018), was employed to determine the climate zone to which each urban cluster belongs. This dataset exhibits a classification accuracy of 80% and has a spatial resolution of 1 km (Beck et al., 2018).

3. Methods

3.1. Methods for estimating UHII

The UHII is defined as the mean temperature difference between the urban area and its BRA. The discrepancies among current UHII estimation methods primarily stem from the selection of BRA, exerting a substantial influence on the magnitude of the estimated UHII (Li et al., 2019b; Liu et al., 2023; Yang et al., 2023b; Yao et al., 2018b). In this study, we proposed the DEA method (i.e. dynamic equal-area method) for identifying the BRA and estimating UHII. This method can efficiently eliminate the influence of confounding factors, including water, topographic relief, and anthropogenic disturbance, on UHII estimates. Importantly, it ensures that the selected BRA possesses enough valid pixels, maintaining a size equivalent to that of the urban area.

3.1.1. Workflow of the DEA method

As shown in Fig. 2, the DEA method mainly comprising the following five steps.

Step 1: Creation of buffer. For an urban cluster with area of A_U, create a buffer around it with radius R. The initial value of R is determined by the area of the urban cluster (see below for details).

Step 2: Removal of confounding factors. For the constructed buffer, remove areas within it that satisfy any of the following conditions: (a) water bodies; (b) areas outside the median elevation of the urban cluster by E_T meters; (c) areas with ISF $\geq ISF_T$; (d) areas with NLI $\geq NLI_T$. Specific values of these parameters are shown below.

Step 3: Update of buffer radius. Calculate the area difference (ΔA) between the urban cluster and the remaining area of the constructed buffer, and update the buffer radius to $R + \Delta R$. Repeat steps 1–3 until $R > R_T$ or ΔA shows opposite signs between consecutive steps.

Step 4: Determination of BRA. Compare the absolute values of the last two iterations of ΔA, and designate the remaining area of the buffer

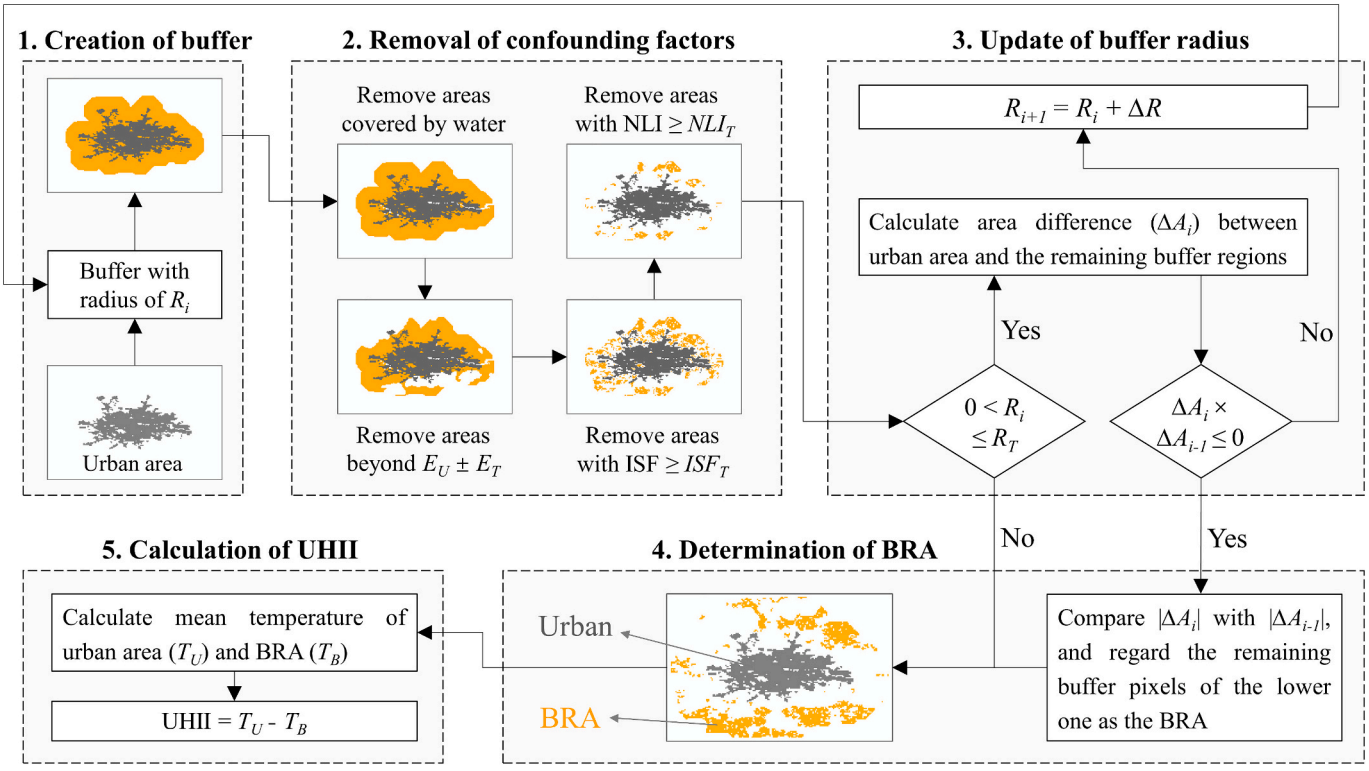

Fig. 2. Flowchart of the dynamic equal-area (DEA) method for estimating UHII. E_T, NLI_T, and ISF_T refer to the upper thresholds of elevation difference from urban median value (E_U), nighttime light intensity (NLI), and impervious surface fraction (ISF), respectively, applied to pixels retained within the background reference area (BRA). R_T represents the upper threshold for the buffer radius. Please refer to Methods section for details of these parameters.

corresponding to the lower value as the final selected BRA.

Step 5: Calculation of UHII. Calculate the mean temperatures of the urban cluster (T_U) and the BRA (T_B), respectively. The estimated UHII is then expressed as: UHII $= T_U - T_B$.

3.1.2. Parameter settings of the DEA method

The initial buffer radius (referred as R_0) is determined by the area of the urban cluster (A_U). Assuming the urban cluster as a disk with the radius of R_U, then the following equation holds:

$$(R_U + R_0)^2 = 2{R_U}^2 \quad (1)$$

$$A_U = \pi {R_U}^2 \quad (2)$$

Jointly solving the above two equations yields that:

$$R_0 = \left(\sqrt{2} - 1\right)\sqrt{A_U/\pi} \quad (3)$$

Construct the buffer using R_0 and calculate the area difference (ΔA_0) between the urban cluster and the buffer. If $\Delta A_0 > 0$ in the initial step, it implies that R_0 takes a lower value, then ΔR should be greater than 0; conversely, ΔR should be lower than 0. Given that the resolution of the LST data is 1 km, we set $|\Delta R| = 1$ km in this study.

To reduce the impact of topographic relief on UHII estimates, we excluded areas beyond the median elevation of the urban cluster by E_T meters from the constructed buffer. Most studies have standardized E_T to 50 m (Du et al., 2023; Imhoff et al., 2010; Lai et al., 2018; Yang and Zhao, 2023; Yang et al., 2023a; Yang et al., 2023b), with a few exceptions opting for alternative thresholds such as100 m (Zhao et al., 2014). In this study, we set E_T at 50 m, a stringent threshold aimed at effectively mitigating the impact of topographic relief, particularly in mountainous cities with significant variations in terrain (Yang et al., 2023b).

To mitigate the influence of anthropogenic disturbance on UHII estimates, we constrained the ISF of all pixels within the BRA to remain below a specified threshold (i.e. ISF_T). Previous UHI-related studies have demonstrated variability in their choice of ISF_T, typically spanning from 5% to 20% (Imhoff et al., 2010; Liu et al., 2023; Yang and Zhao, 2023; Yang et al., 2023a; Yao et al., 2018b; Zhou et al., 2016). In this study, we applied a relatively stringent ISF_T of 5%, as this is the most commonly used threshold (Yao et al., 2018b).

Following the study of Li et al. (2022), we excluded pixels with relatively high NLI from the BRA to further mitigate the influence of anthropogenic activities. Compared to the previous study, we implemented a stricter exclusion criterion by setting the upper threshold for NLI (i.e. NLI_T) to be 1 nW/cm^2/sr for all areas within the BRA. We set NLI_T as this value because previous studies have indicated that NLIs below than 1 nW/cm^2/sr were predominantly associated with background noise (Chen et al., 2021; Zhao et al., 2020; Zheng et al., 2019). This low threshold for NLI helps maximize the confidence in our selected BRA to represent the natural surface state.

The DEA method dynamically adapts the buffer radius to eliminate confounding factors while ensuring that the selected BRA retain enough valid pixels. Meanwhile, the BRA should not be too distant from the urban area, as remote pixels might reflect different climate regimes (Luo and Lau, 2018). Hence, we set the maximum threshold (i.e. R_T) for the buffer radius to 100 km, and areas beyond this limit will be excluded from the BRA. This setting of the maximum buffer radius is consistent with that used in recent UHI-related studies (Du et al., 2023; Luo and Lau, 2018).

We have conducted a thorough analysis of the potential impacts of variations in the above threshold parameters (E_T, ISF_T, NLI_T, and R_T) on UHII estimates. Please refer to Section 5.4 for detailed information regarding the sensitivity analysis of these parameters.

3.1.3. Methods for comparative analysis

To validate the effectiveness of our proposed DEA method, we conducted a comparative analysis with three other commonly used area-based buffer methods.

(1) EA method: The equal-area (EA) method stands as one of the most employed methods for UHII estimation (Peng et al., 2012; Zhou et al., 2018; Zhou et al., 2014). This method establishes the BRA by creating a buffer around the urban area of equal size. Similar to our DEA method, the EA method also excludes areas within the BRA that are affected by water bodies and/or topographic relief.
(2) IEA method: Building upon the BRA extracted by the EA method, it is necessary to further exclude areas influenced by anthropogenic disturbance. Typically, areas with the ISF higher than 5% within the BRA are identified for removal (Imhoff et al., 2010; Yao et al., 2018b). This approach is denoted as the IEA method.
(3) MEA method: The modified equal-area (MEA) method proposed by Li et al. (2022) seeks to reduce anthropogenic disturbance by removing areas with high NLI within the BRA. The first step of the MEA method involves mitigating the influences of water bodies and topographic relief and creating a buffer twice the size of the urban area. The subsequent step is to exclude areas within the buffer where the NLI exceeds its median value.

3.2. Generation and analysis of our UHII dataset

3.2.1. Generation of a global, long-term, and multi-faceted UHII dataset

Based on the proposed DEA method, we obtained the UHII of 10,196 global cities (or urban clusters) to create a UHII dataset. This dataset comprises the UHII values derived from eight different sources of temperature data, and they describe aspects of the UHI effect (Table 1). The UHII values derived from the original MODIS LST data, including I_{Mod1} (i.e., UHII from the Mod1 data, hereinafter), I_{Mod2}, I_{Myd1}, and I_{Myd2}, represent the surface UHII under clear-sky conditions. I_{SMod2} and I_{SMyd1} were derived from the gap-filed MODIS LST data, representing the clear-sky surface UHII without the influence of missing data. I_{AMod2} was obtained by using the seamless all-sky LST data, providing an assessment of surface UHII under all-sky conditions. I_{SAT} was computed using gridded SAT data and represents the canopy UHII. All the mentioned UHII indicators include monthly values, seasonal averages, and annual averages for each year during their respective accessible periods (Table 1).

3.2.2. Global analysis and comparison of the magnitude and trend of UHII

Utilizing the derived UHII dataset, we examined the spatiotemporal patterns and inter-annual trends of UHII. To ensure a fair comparison, the analysis was confined to the time frame (2003−2020) covered by all available data. First, we computed the average UHII for each city from 2003 to 2020 as a representative measure of the magnitude of UHI signal. Subsequently, we analyzed the UHII trend across years for each city using the Mann-Kendall (MK) and Sen's slope estimator tests (Yang

Table 1
UHII indicators derived from different temperature data.

Indicator	Data source	Period	Time	Data Provider
Surface UHI intensity estimated by the clear-sky LST data				
I_{Mod1}	MOD11A1 (Mod1)	2001–2021	~10:30 & ~22:30	NASA
I_{Mod2}	MOD11A2 (Mod2)			
I_{Myd1}	MYD11A1 (Myd1)	2003–2021	~13:30 & ~1:30	
I_{Myd2}	MYD11A2 (Myd2)			
Surface UHI intensity estimated by the seamless clear-sky LST data				
I_{SMod2}	Seamless MOD11A2 (SMod2)	2001–2020	~10:30 & ~22:30	Yao et al. (2023)
I_{SMyd1}	Seamless MYD11A1 (SMyd1)	2003–2020	~13:30 & ~1:30	Zhang et al. (2023)
Surface UHI intensity estimated by the seamless all-sky LST data				
I_{AMod2}	All-sky MOD11A2 (AMod2)	2001–2020	~10:30 & ~22:30	Yao et al. (2023)
Canopy UHI intensity estimated by the gridded surface air temperature data				
I_{SAT}	Surface air temperature (SAT)	2001–2020	Max & Min	Yao et al. (2023)

et al., 2019; Yao et al., 2019). On this basis, we made a thorough analysis of the spatial, diurnal, and seasonal patterns of the magnitude and trend of UHII, as well as the relationship between them. Besides, we conducted a detail comparison of the UHII derived from different sources of temperature data.

4. Results

4.1. Performance evaluations of the DEA method

Fig. 3 illustrates the spatial extent of the BRA and the average values of ISF and NLI within it obtained through different methods. It is evident that, in comparison to the traditional EA method, the IEA method can largely reduce the ISF within BRAs, while the MEA method can substantially diminish the NLI within the BRAs. Our proposed DEA method combines the advantages of IEA and MEA methods, proving more effective in simultaneously reducing ISF and NLI within the BRA. Therefore, the BRA obtained by the DEA method is expected to be less influenced by anthropogenic disturbance and more representative of the natural background climate compared to those obtained by other methods.

Consequently, the UHII estimated by the DEA method is typically higher than that estimated by other methods (Table 2 & Fig. S1). On average for global cities, the UHII derived from the DEA method surpasses that of the EA method by more than 50% and is about 10% higher than that of the IEA (or MEA) method (Table 2). This is attributed to the effectiveness of the BRA selected by the DEA method, which systematically excludes areas with elevated temperatures associated with anthropogenic activities. As a result, the DEA method can effectively emphasize the temperature difference between the urban area and its background. Additionally, the trend of UHII derived from the DEA method is also more pronounced compared to that of other methods (Table 3). Globally, the UHII trend of the DEA method surpasses that of the IEA (or MEA) method by more than 25% during the daytime and over 40% during the nighttime. The UHII trend of the EA method is the lowest, reaching only about 1/10 to 1/5 of the UHII trend obtained by the DEA method (Table 3). This suggests that the influence of anthropogenic disturbance within the BRA can obscure the true trend of UHII, and the DEA method, which eliminates this influence, can better highlight the UHII trend.

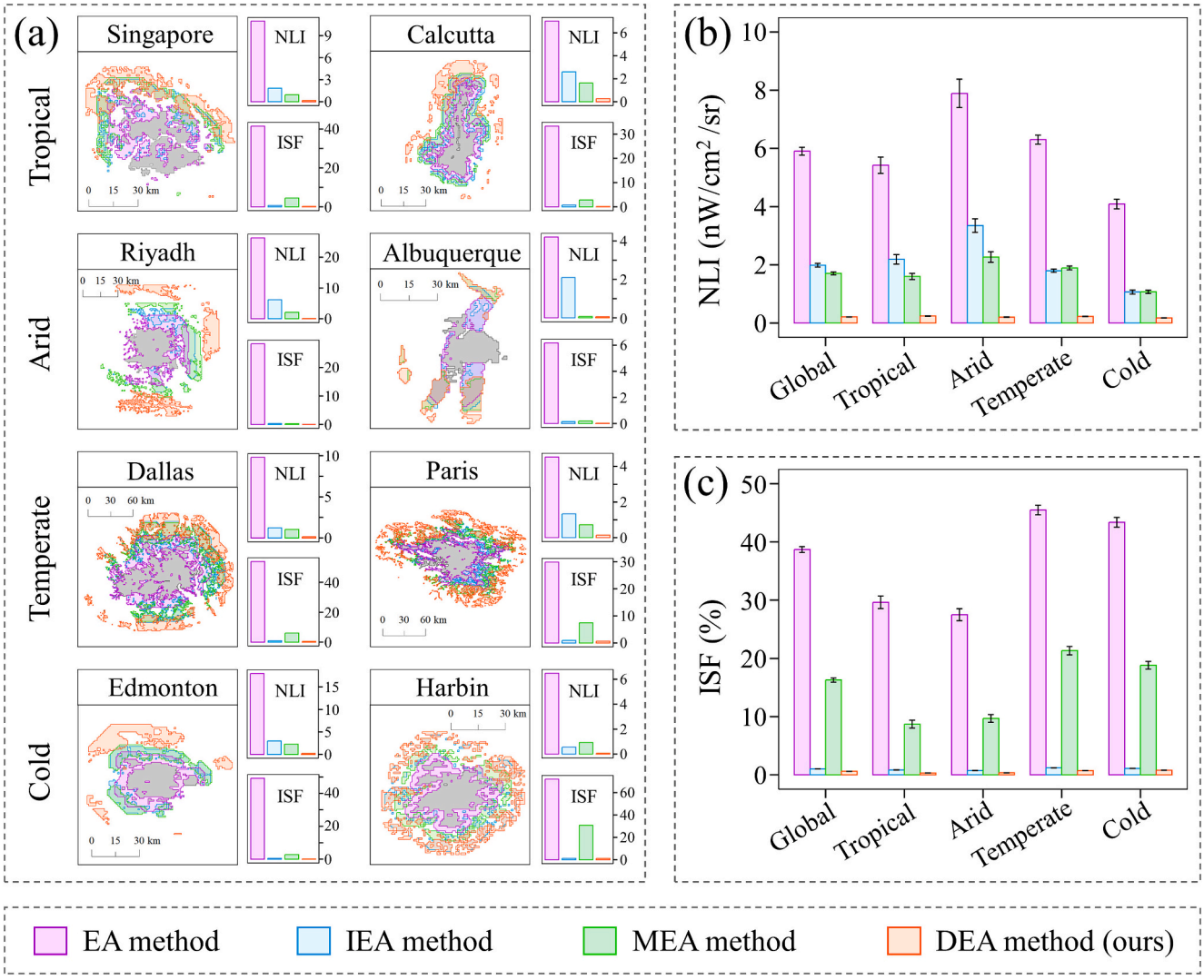

Fig. 3. Comparisons of different methods, including EA, IEA, MEA, and DEA, for delineating the background reference area (BRA). (a) Spatial extents of BRAs and the mean values of nighttime light intensity (NLI) and impervious surface fraction (ISF) within them in eight representative cities. (b) Mean values (95% confidence intervals) of NLI within BRAs for global cities as well as for cities located in different climate zones. (c) Mean values (95% confidence intervals) of ISF within BRAs for global cities as well as cities located in different climate zones. The comparison above is presented as an illustrative example from the year 2020. Please refer to the Methods section for detailed explanations of each method.

Table 2
Global averages (± 95% confidence intervals) of the magnitude of UHII estimated by different temperature data and methods. The magnitude is calculated as the average of UHII during 2003–2020. The magnitude of UHII estimated by the DEA method (bold) is significantly ($p < 0.05$, *t*-test) higher than that of other methods.

Period	Method	Magnitudes of UHII derived from different temperature datasets (°C)							
		I_{Mod1}	I_{Mod2}	I_{Myd1}	I_{Myd2}	I_{SMod2}	I_{SMyd1}	I_{AMod2}	I_{SAT}
Annual day	EA	0.584 ± 0.015	0.581 ± 0.015	0.783 ± 0.016	0.774 ± 0.016	0.554 ± 0.015	0.653 ± 0.017	0.550 ± 0.014	0.298 ± 0.006
	IEA	0.881 ± 0.022	0.876 ± 0.022	1.177 ± 0.025	0.163 ± 0.025	0.835 ± 0.022	1.020 ± 0.025	0.829 ± 0.022	0.427 ± 0.008
	MEA	0.820 ± 0.021	0.815 ± 0.021	1.108 ± 0.025	1.094 ± 0.025	0.776 ± 0.020	0.956 ± 0.025	0.770 ± 0.020	0.407 ± 0.007
	DEA	**0.941 ± 0.025**	**0.934 ± 0.025**	**1.256 ± 0.031**	**1.239 ± 0.031**	**0.890 ± 0.025**	**1.125 ± 0.030**	**0.881 ± 0.025**	**0.457 ± 0.008**
Annual night	EA	0.567 ± 0.009	0.559 ± 0.009	0.495 ± 0.008	0.490 ± 0.008	0.544 ± 0.09	0.463 ± 0.008	0.546 ± 0.009	0.312 ± 0.004
	IEA	0.774 ± 0.011	0.763 ± 0.011	0.682 ± 0.010	0.673 ± 0.010	0.745 ± 0.011	0.651 ± 0.010	0.746 ± 0.011	0.435 ± 0.006
	MEA	0.748 ± 0.010	0.737 ± 0.010	0.658 ± 0.010	0.649 ± 0.010	0.719 ± 0.010	0.627 ± 0.010	0.720 ± 0.010	0.417 ± 0.005
	DEA	**0.832 ± 0.12**	**0.820 ± 0.012**	**0.736 ± 0.012**	**0.726 ± 0.012**	**0.802 ± 0.012**	**0.708 ± 0.012**	**0.801 ± 0.012**	**0.473 ± 0.008**
Summer day	EA	0.914 ± 0.022	0.911 ± 0.022	1.171 ± 0.025	1.166 ± 0.025	0.871 ± 0.020	1.099 ± 0.024	0.860 ± 0.020	0.367 ± 0.006
	IEA	1.421 ± 0.031	1.415 ± 0.031	1.816 ± 0.037	1.808 ± 0.037	1.348 ± 0.029	1.620 ± 0.035	1.330 ± 0.030	0.543 ± 0.010
	MEA	1.308 ± 0.029	1.302 ± 0.029	1.690 ± 0.035	1.682 ± 0.035	1.240 ± 0.029	1.505 ± 0.034	1.223 ± 0.028	0.514 ± 0.010
	DEA	**1.518 ± 0.037**	**1.510 ± 0.037**	**1.938 ± 0.043**	**1.928 ± 0.043**	**1.434 ± 0.035**	**1.746 ± 0.040**	**1.412 ± 0.035**	**0.583 ± 0.012**
Summer night	EA	0.628 ± 0.008	0.612 ± 0.008	0.522 ± 0.008	0.512 ± 0.008	0.572 ± 0.008	0.472 ± 0.008	0.571 ± 0.008	0.290 ± 0.006
	IEA	0.886 ± 0.013	0.863 ± 0.013	0.744 ± 0.012	0.730 ± 0.011	0.810 ± 0.012	0.690 ± 0.011	0.806 ± 0.012	0.418 ± 0.008
	MEA	0.845 ± 0.012	0.824 ± 0.012	0.709 ± 0.010	0.695 ± 0.010	0.771 ± 0.010	0.657 ± 0.011	0.769 ± 0.010	0.395 ± 0.007
	DEA	**0.959 ± 0.014**	**0.934 ± 0.014**	**0.813 ± 0.012**	**0.797 ± 0.012**	**0.876 ± 0.012**	**0.760 ± 0.012**	**0.871 ± 0.012**	**0.459 ± 0.008**
Winter day	EA	0.303 ± 0.012	0.307 ± 0.012	0.451 ± 0.016	0.449 ± 0.016	0.292 ± 0.012	0.421 ± 0.016	0.293 ± 0.012	0.229 ± 0.006
	IEA	0.428 ± 0.016	0.435 ± 0.016	0.646 ± 0.022	0.645 ± 0.022	0.415 ± 0.016	0.608 ± 0.022	0.415 ± 0.016	0.314 ± 0.006
	MEA	0.411 ± 0.016	0.418 ± 0.016	0.622 ± 0.020	0.621 ± 0.020	0.398 ± 0.016	0.588 ± 0.022	0.398 ± 0.016	0.304 ± 0.006
	DEA	**0.462 ± 0.020**	**0.470 ± 0.020**	**0.695 ± 0.024**	**0.694 ± 0.024**	**0.449 ± 0.020**	**0.662 ± 0.024**	**0.448 ± 0.020**	**0.337 ± 0.008**
Winter night	EA	0.520 ± 0.010	0.515 ± 0.010	0.469 ± 0.010	0.464 ± 0.010	0.512 ± 0.008	0.437 ± 0.010	0.517 ± 0.008	0.333 ± 0.006
	IEA	0.683 ± 0.012	0.675 ± 0.012	0.621 ± 0.014	0.612 ± 0.014	0.677 ± 0.012	0.592 ± 0.014	0.682 ± 0.013	0.452 ± 0.009
	MEA	0.671 ± 0.012	0.664 ± 0.012	0.609 ± 0.014	0.600 ± 0.012	0.663 ± 0.012	0.579 ± 0.012	0.668 ± 0.012	0.438 ± 0.008
	DEA	**0.728 ± 0.014**	**0.720 ± 0.014**	**0.662 ± 0.016**	**0.652 ± 0.016**	**0.723 ± 0.014**	**0.635 ± 0.014**	**0.728 ± 0.014**	**0.490 ± 0.010**

Table 3
Global averages (± 95% confidence intervals) of the trend of UHII estimated by different temperature data and methods. The trend denotes the change rate of UHII estimated based on year-by-year values during 2003–2020. The trend of UHII estimated by the DEA method (bold) is significantly ($p < 0.05$, t-test) higher than that of other methods.

Period	Method	Trends of UHII derived from different temperature datasets (°C/decade)							
		I_{Mod1}	I_{Mod2}	I_{Myd1}	I_{Myd2}	I_{SMod2}	I_{SMyd1}	I_{AMod2}	I_{SAT}
Annual day	EA	0.022 ± 0.004	0.023 ± 0.004	0.024 ± 0.004	0.026 ± 0.004	0.018 ± 0.003	0.024 ± 0.004	0.017 ± 0.003	−0.004 ± 0.001
	IEA	0.108 ± 0.006	0.110 ± 0.006	0.137 ± 0.008	0.138 ± 0.008	0.092 ± 0.006	0.129 ± 0.008	0.089 ± 0.006	0.024 ± 0.002
	MEA	0.093 ± 0.006	0.094 ± 0.006	0.111 ± 0.008	0.113 ± 0.008	0.079 ± 0.005	0.104 ± 0.006	0.076 ± 0.005	0.020 ± 0.002
	DEA	**0.135 ± 0.012**	**0.137 ± 0.012**	**0.162 ± 0.012**	**0.163 ± 0.012**	**0.112 ± 0.010**	**0.157 ± 0.012**	**0.106 ± 0.010**	**0.032 ± 0.004**
Annual night	EA	0.005 ± 0.002	0.002 ± 0.002	0.013 ± 0.002	0.013 ± 0.002	−0.000 ± 0.001	0.013 ± 0.002	−0.000 ± 0.001	0.000 ± 0.001
	IEA	0.051 ± 0.004	0.047 ± 0.004	0.055 ± 0.004	0.053 ± 0.004	0.042 ± 0.004	0.056 ± 0.004	0.041 ± 0.004	0.025 ± 0.002
	MEA	0.045 ± 0.004	0.042 ± 0.004	0.057 ± 0.004	0.055 ± 0.004	0.037 ± 0.003	0.056 ± 0.004	0.037 ± 0.003	0.022 ± 0.002
	DEA	**0.073 ± 0.006**	**0.069 ± 0.006**	**0.082 ± 0.006**	**0.080 ± 0.006**	**0.063 ± 0.004**	**0.084 ± 0.006**	**0.061 ± 0.004**	**0.039 ± 0.004**
Summer day	EA	0.053 ± 0.006	0.054 ± 0.006	0.071 ± 0.006	0.072 ± 0.006	0.052 ± 0.004	0.068 ± 0.008	0.049 ± 0.004	−0.001 ± 0.002
	IEA	0.202 ± 0.008	0.205 ± 0.008	0.265 ± 0.010	0.266 ± 0.010	0.180 ± 0.008	0.247 ± 0.012	0.174 ± 0.008	0.037 ± 0.004
	MEA	0.177 ± 0.010	0.180 ± 0.010	0.218 ± 0.012	0.219 ± 0.012	0.160 ± 0.008	0.199 ± 0.012	0.154 ± 0.008	0.033 ± 0.004
	DEA	**0.238 ± 0.016**	**0.241 ± 0.016**	**0.294 ± 0.018**	**0.297 ± 0.018**	**0.204 ± 0.016**	**0.282 ± 0.016**	**0.193 ± 0.014**	**0.047 ± 0.006**
Summer night	EA	0.023 ± 0.002	0.018 ± 0.002	0.022 ± 0.002	0.022 ± 0.002	0.008 ± 0.002	0.017 ± 0.002	0.007 ± 0.002	0.005 ± 0.001
	IEA	0.082 ± 0.004	0.075 ± 0.004	0.073 ± 0.004	0.071 ± 0.004	0.057 ± 0.004	0.067 ± 0.004	0.055 ± 0.004	0.031 ± 0.002
	MEA	0.073 ± 0.004	0.067 ± 0.004	0.072 ± 0.004	0.071 ± 0.004	0.050 ± 0.004	0.066 ± 0.004	0.048 ± 0.004	0.028 ± 0.002
	DEA	**0.106 ± 0.006**	**0.099 ± 0.006**	**0.104 ± 0.006**	**0.102 ± 0.006**	**0.078 ± 0.006**	**0.100 ± 0.006**	**0.073 ± 0.006**	**0.044 ± 0.004**
Winter day	EA	−0.007 ± 0.004	−0.007 ± 0.004	−0.021 ± 0.004	−0.019 ± 0.004	−0.012 ± 0.004	−0.020 ± 0.006	−0.012 ± 0.004	−0.015 ± 0.002
	IEA	0.015 ± 0.006	0.016 ± 0.006	0.013 ± 0.008	0.018 ± 0.008	0.004 ± 0.006	0.011 ± 0.008	0.004 ± 0.006	−0.005 ± 0.002
	MEA	0.017 ± 0.006	0.018 ± 0.006	0.013 ± 0.008	0.017 ± 0.008	0.009 ± 0.006	0.013 ± 0.008	0.009 ± 0.006	−0.005 ± 0.002
	DEA	**0.038 ± 0.010**	**0.042 ± 0.010**	**0.040 ± 0.012**	**0.047 ± 0.012**	**0.027 ± 0.008**	**0.045 ± 0.010**	**0.026 ± 0.008**	**0.005 ± 0.003**
Winter night	EA	−0.007 ± 0.002	−0.008 ± 0.002	0.006 ± 0.002	0.005 ± 0.002	−0.005 ± 0.002	0.007 ± 0.002	−0.005 ± 0.002	−0.003 ± 0.002
	IEA	0.026 ± 0.004	0.023 ± 0.004	0.036 ± 0.004	0.033 ± 0.006	0.028 ± 0.004	0.038 ± 0.004	0.028 ± 0.004	0.020 ± 0.003
	MEA	0.024 ± 0.004	0.022 ± 0.004	0.042 ± 0.004	0.039 ± 0.004	0.028 ± 0.004	0.042 ± 0.004	0.027 ± 0.004	0.019 ± 0.003
	DEA	**0.042 ± 0.006**	**0.040 ± 0.006**	**0.056 ± 0.008**	**0.053 ± 0.008**	**0.048 ± 0.006**	**0.057 ± 0.006**	**0.047 ± 0.006**	**0.036 ± 0.004**

Overall, our proposed DEA method demonstrates superior effectiveness in mitigating anthropogenic disturbance during the BRA selection. Consequently, the UHII estimated by the DEA method more effectively underscores the impact of urbanization on local temperature. Given the advantages of the DEA method, the subsequent analysis will be grounded in its outcomes.

4.2. Magnitudes and trends of UHII

4.2.1. Magnitudes of UHII

The majority of cities worldwide exhibit a UHII greater than zero, with over 80% experiencing it during the day and over 90% at night (Figs. 4–5). Cities with UHII lower than zero are primarily concentrated in the Middle East and North Africa (Figs. 4–5). On average, for global cities, the annual daytime surface UHII is around 1 °C (0.881–1.239 °C, depending on the temperature data), which is significantly ($p < 0.05$, t-test) higher than that during annual nighttime (0.708–0.832 °C) (Table 2). While the annual nighttime canopy UHII exhibits a slightly stronger magnitude than the annual daytime canopy UHII for their global averages (0.473 °C versus 0.457 °C) (Table 2). In terms of seasonal variation, the surface UHII generally shows stronger magnitude in summer compared to winter for both daytime and nighttime global averages (Fig. 6). In contrast, the canopy UHII follows a similar seasonal pattern (summer > winter) for daytime global averages but an opposite pattern for nighttime global averages (Fig. 6).

The magnitude of UHII displays noticeable variation across climatic zones (Figs. 4–5), with changes in diurnal and seasonal patterns (Fig. 6). Both surface and canopy UHIIs have their lowest average magnitudes in the arid zone, while they are much stronger in tropical, temperate, and cold zones during annual daytime (Fig. 4b). Conversely, during annual nighttime, arid cities experience the highest average magnitudes of surface and canopy UHIIs, followed by cities located in cold, temperate, and tropical zones (Fig. 5b). This leads to variations in the diurnal patterns of UHII among climate zones, with tropical cities exhibiting the strongest positive day-night difference, while arid cities experience the lowest negative day-night difference. In addition, discrepancies are observed in the seasonal patterns of UHII across various climate zones (Fig. 6). In the tropical zone, surface UHII exhibits opposing seasonal patterns between daytime (summer > winter) and nighttime (summer < winter) averages, while canopy UHII is higher in winter than summer for both daytime and nighttime averages (Fig. 6). In the arid zone, daytime UHIIs (surface and canopy) peak in spring and decline to their lowest levels in autumn, while nighttime UHIIs reach their lowest values in summer (Fig. 6). In the temperate and cold zones, both surface and canopy UHIIs exhibit higher average magnitudes during summer compared to winter, regardless of whether it is daytime or nighttime (Fig. 6).

4.2.2. Trends of UHII

Over 60% of the global cities exhibit an increasing trend in UHII, with approximately half of these cities displaying significant ($p < 0.05$, MK test) growth trends (Figs. 7–8). On average, for global cities, the annual daytime surface UHII trend exceeds 0.1 °C/decade (0.106–0.163 °C/decade), approximately twice the corresponding nighttime surface UHII trend (0.061–0.082 °C/decade) (Table 3). In contrast, the trend of annual nighttime canopy UHII appears to be slightly stronger than that during annual daytime (0.039 °C/decade versus 0.032 °C/decade) (Table 3). Seasonally, surface and canopy UHIIs consistently display stronger magnitudes in summer compared to winter for both daytime and nighttime global averages (Fig. 9).

Spatially, cities with higher UHII trends are concentrated in the tropical and temperate climate zones, while the trend is negative in some cities located in the arid and cold climate zones (Figs. 7–8). On average, annual daytime UHIIs (surface and canopy) have their lowest and negative trends in the arid zone, minor but positive trends in the cold zone, and much stronger trends in the tropical and temperate zones (Fig. 7b). Conversely, during annual nighttime, the highest average trends are observed in the arid or tropical zones, followed by cities located in the temperate and cold zones (Fig. 8b). Similar to the magnitude of UHII, the trend of UHII also exhibits different seasonal patterns among climate zones (Fig. 9). In the tropical zone, the trends of surface UHII are averagely higher in summer than in winter during daytime, while the opposite is observed during nighttime (Fig. 9). However, for averages of tropical cities, the trends of canopy UHII appear consistent across seasons during daytime but show evident differences between summer and winter at nighttime (Fig. 9). In the arid zone, the average trends of surface UHII are much higher in winter than summer, while a weak but opposite seasonal pattern is observed for the average trends of daytime canopy UHII (Fig. 9). Furthermore, for cities located in the temperate and cold zones, the average trends of UHII are higher in summer compared to winter, which remains consistent for both surface and canopy UHIIs (Fig. 9).

4.2.3. Associations between the magnitude and trend of UHII

We observe a significant ($p < 0.05$) positive correlation between the magnitude and trend of UHII (Fig. 10), suggesting that cities with stronger UHII have experienced faster growth in UHII over recent decades. This positive correlation holds true for all UHII indicators, with surface UHII showing a stronger association compared to canopy UHII (Fig. 10). Besides, daytime UHII exhibits a closer association between magnitude and trend compared to nighttime UHII (Fig. 10). Additionally, the UHII and its trends share the same sign in most cities (about 2/3) (Fig. 10), implying that cities with positive magnitude of UHII also tend to exhibit positive trend of UHII, and vice versa.

4.3. Comparisons of UHII derived from various temperature data

4.3.1. Terra vs. Aqua

The Aqua overpass is closer to the daily peak of LST compared to Terra. As a result, the UHII derived from the Aqua LST ($I_{Myd,}$ specifically I_{Myd1} or I_{Myd2}) demonstrates a higher daytime magnitude and a lower nighttime magnitude compared to the surface UHII derived from the Terra LST ($I_{Mod,}$ specifically I_{Mod1} or I_{Mod2}) (Figs. 4–5). Globally, the average magnitude of I_{Myd} is approximately 30% higher than I_{Mod} during annual daytime and roughly 10% lower than I_{Mod} during annual nighttime. Moreover, the trends of UHII derived from the Aqua LST tend to surpass that of the Terra LST (Figs. 7–8). Globally, the annual daytime and nighttime trends of I_{Myd} are approximately 20% and 10% higher, respectively, than the trends of I_{Mod}. Besides, both the magnitude and trend of I_{Myd} exhibit more pronounced variations than I_{Mod} in terms of seasonal and diurnal differences (Figs. 6, 9). These results demonstrate that the Aqua LST appears more advantageous in capturing the spatial and temporal variations of UHII compared to the Terra LST.

4.3.2. Daily LST vs. 8-day composite LST

The comparison indicates a close resemblance between the UHII derived from daily LST (I_{Mod1} or I_{Myd1}) and the UHII derived from 8-day composite LST (I_{Mod2} or I_{Myd2}). While the global average magnitude of I_{Mod1} (I_{Myd1}) is slightly higher than that of I_{Mod2} (I_{Myd2}), the difference between them is not statistically significant ($p > 0.05$, t-test) (Figs. 4–5). Likewise, the differences between the trend of I_{Mod1} and the trend of I_{Mod2}, as well as the trend of I_{Myd1} and the trend of I_{Myd2}, are not found to be significant ($p > 0.05$, t-test) (Figs. 7–8). The above results demonstrate that studying UHII at annual- or seasonal-averaged scales yields very similar outcomes whether using daily LST or 8-day composite LST. Consequently, opting for 8-day composite LST appears to be a more favorable choice for such UHI studies in terms of saving data processing complexity.

4.3.3. Original LST vs. seamless LST

Spatiotemporally seamless LST can be achieved through the interpolation of the original clear-sky LST data with gaps. The resulting seamless LST is categorized into two groups, namely the seamless clear-sky LST and the seamless all-sky LST, based on whether the interpolation method considers weather conditions. Comparison results reveal that the UHII derived from the original LST is generally stronger than that based on seamless clear-sky or all-sky LST. Globally, the average magnitude of I_{Mod2} (based on the original clear-sky LST) is higher than I_{SMod2} (based on the seamless clear-sky LST) or I_{AMod2} (based on

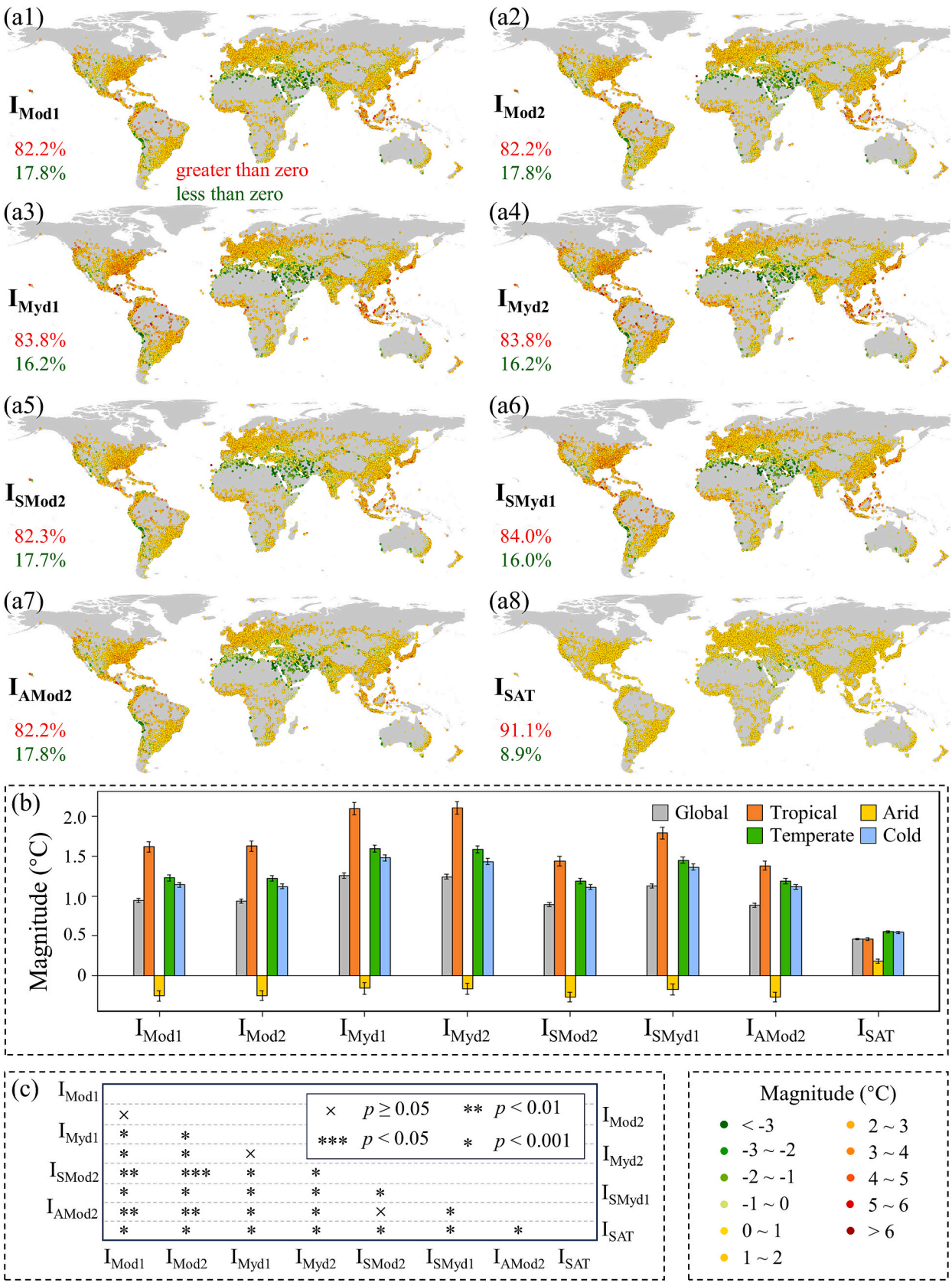

Fig. 4. Magnitudes of annual daytime UHII derived from different temperature data. (a1-a8) Spatial patterns across global cities. (b) Mean values (95% confidence intervals) for different climate zones and for the globe. (c) Mutual comparisons through *t*-tests. The magnitude is calculated as the average of UHII during 2003–2020. Please refer to Table 1 for specific details about each UHII indicator.

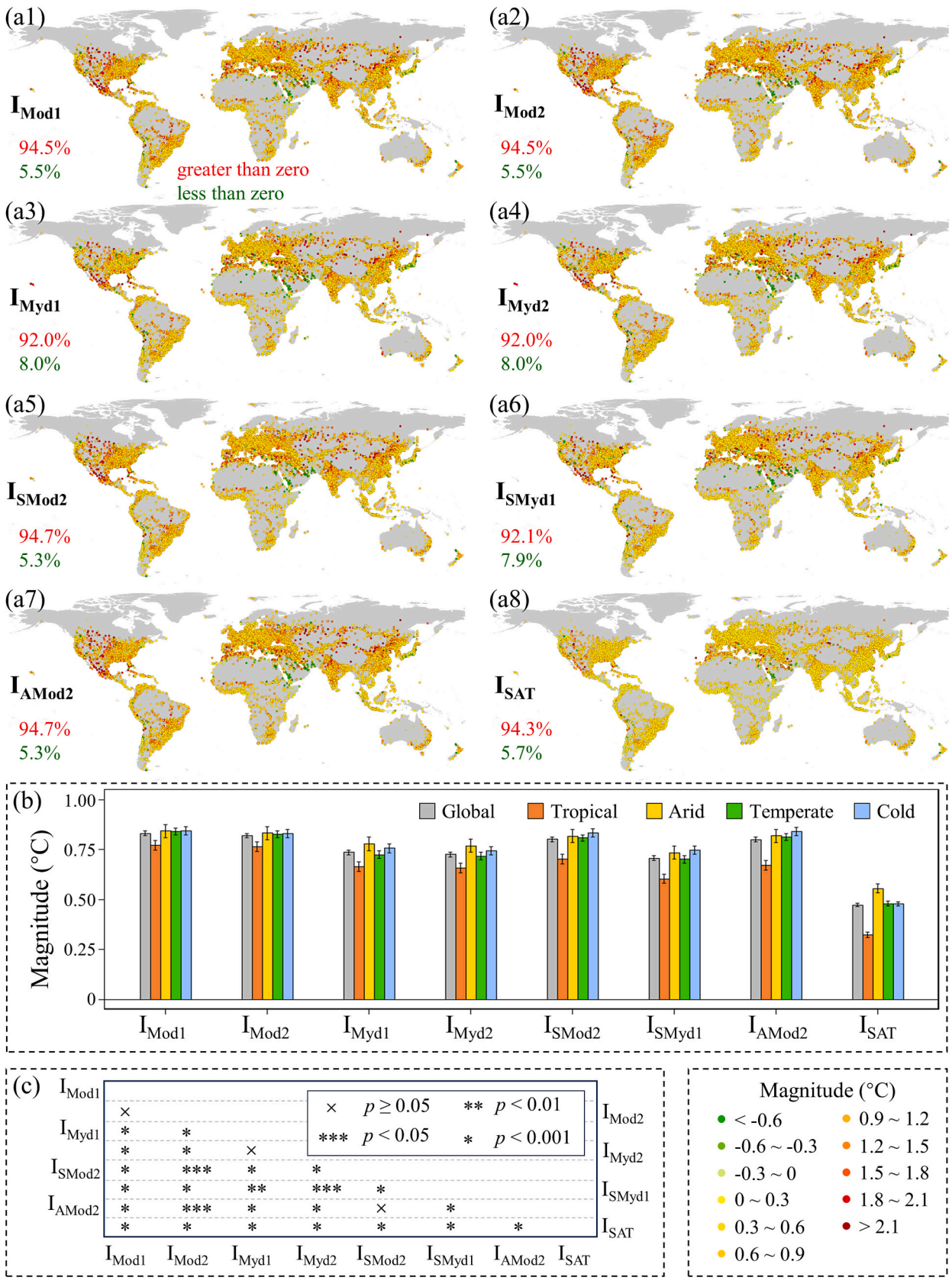

Fig. 5. Same as Fig. 4, but for annual nighttime UHII.

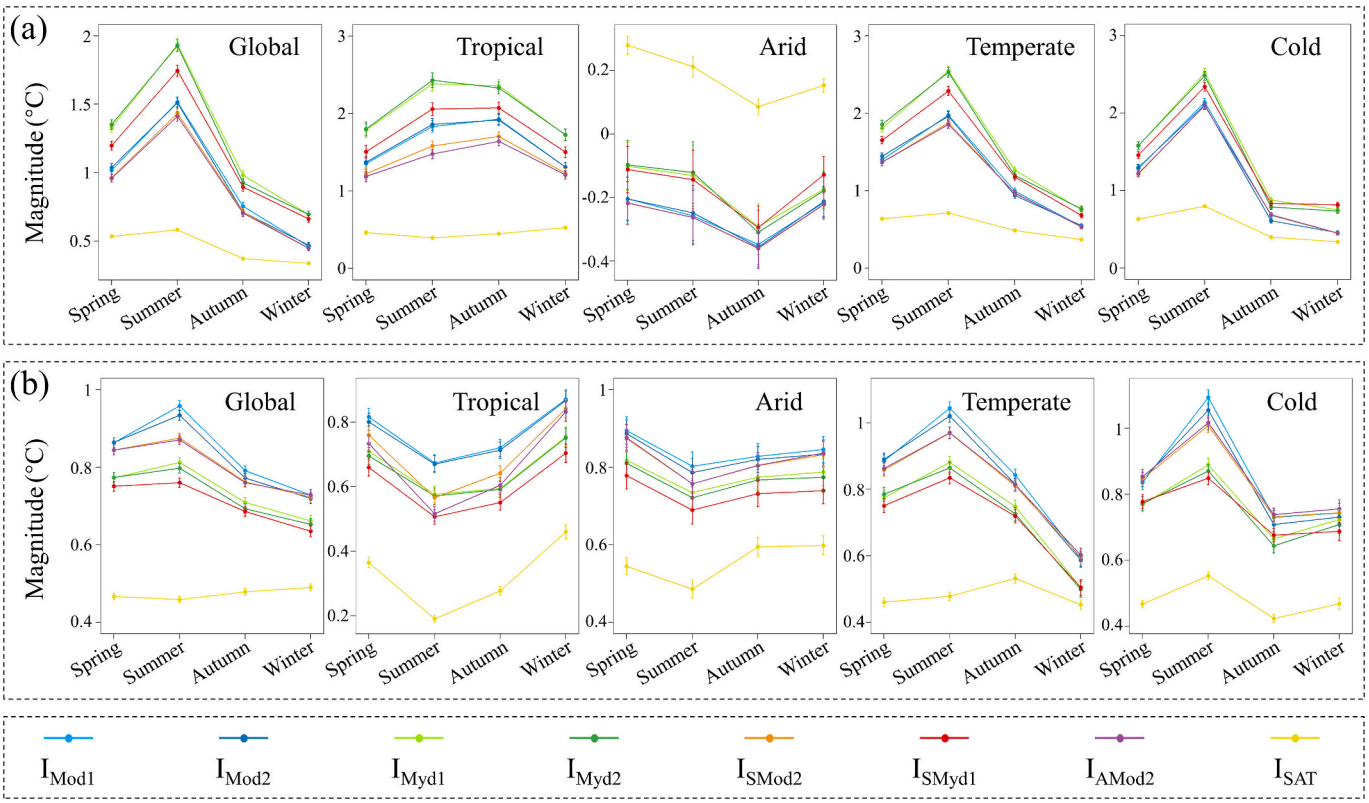

Fig. 6. Seasonal variations of the magnitude of UHII derived from different temperature data. (a) Daytime results. (b) Nighttime results. The magnitude is calculated as the average of UHII during 2003–2020. Colored points and error bars represent the averages and 95% confidence intervals, respectively. Please refer to Table 1 for specific details about each UHII indicator.

seamless all-sky LST) by about 5% and 2% during annual daytime and nighttime, respectively (Figs. 4–5). Meanwhile, the average trend of I_{Mod2} is higher than the trends of I_{SMod2} and I_{AMod2} by approximately 20% and 30%, respectively, during annual daytime, and by about 5% during annual nighttime (Figs. 7–8). Additionally, it has been observed that the discrepancies between the UHII derived from the original LST and that derived from seamless LST are more pronounced during the summertime (Figs. 6, 9). The above results suggest that the UHII estimated based on the original LST with gaps may overestimate the surface UHI effect. The use of seamless LST data, in contrast, can significantly reduce the bias in the quantification of UHII caused by missing data.

4.3.4. LST vs. SAT

The magnitude and trend of surface UHII, derived from LST, are both higher and exhibit greater spatial heterogeneity compared to canopy UHII, derived from SAT. On global average, the magnitude of surface UHII is about 2–3 times and 1.5–2 times higher than that of canopy UHII during annual daytime and nighttime, respectively (Figs. 4–5). Meanwhile, the trend of surface UHII is about 3–5 times and 1.5–2 times higher than that of canopy UHII during annual daytime and nighttime, respectively (Figs. 7–8). Additionally, both the magnitude and trend of surface UHII exhibit greater seasonal variations compared to canopy UHII. Globally, the summer-winter difference in the magnitude and trend of daytime surface UHII can reach more than 5 times the canopy UHII (Figs. 6, 9). These results underscore the substantial discrepancies between surface and canopy UHIIs, suggesting a potential overestimation of human perceived UHII when derived from remotely sensed LST (Venter et al., 2021).

5. Discussion

5.1. Implications of this study in terms of methodology, dataset, and analysis

(1) This study introduces a new method for more accurate estimation of UHII.

Accurate quantification of UHII is a fundamental requirement for studying the urban thermal environment (Li et al., 2019b; Liu et al., 2023; Yang et al., 2023b). Several methods for UHII estimation have been proposed in previous studies, which differ mainly in the selection of the BRA. Traditional BRA selection methods can be broadly categorized into distance-based and area-based methods (Li et al., 2019b; Yang et al., 2023b). Area-based methods consider the size of the city itself in the BRA selection, making them suitable for large-scale UHI studies that encompass cities of different sizes (Lai et al., 2018). Moreover, it is crucial to select a BRA that minimizes the influence of confounding factors, including both natural influences (such as water bodies and topographic relief) and anthropogenic disturbance (such as man-made surfaces and human activities) (Li et al., 2022). These confounding factors can introduce anomalies in the BRA temperature, potentially reducing the full UHI signal. Most existing area-based methods have effectively eliminated natural influences when extracting the BRA, but have overlooked the anthropogenic disturbance (Peng et al., 2012; Yang et al., 2017; Zhou et al., 2014). Recently, Li et al. (2022) proposed a method for removing the anthropogenic disturbance by excluding areas in the BRA with excessive NLI. Our study draws on this idea and further incorporates the ISF to propose a new method for quantifying UHII, termed the DEA method. This method can minimize the influence of various confounding factors through a dynamic cyclic process. The comparative results indicate that our proposed DEA method

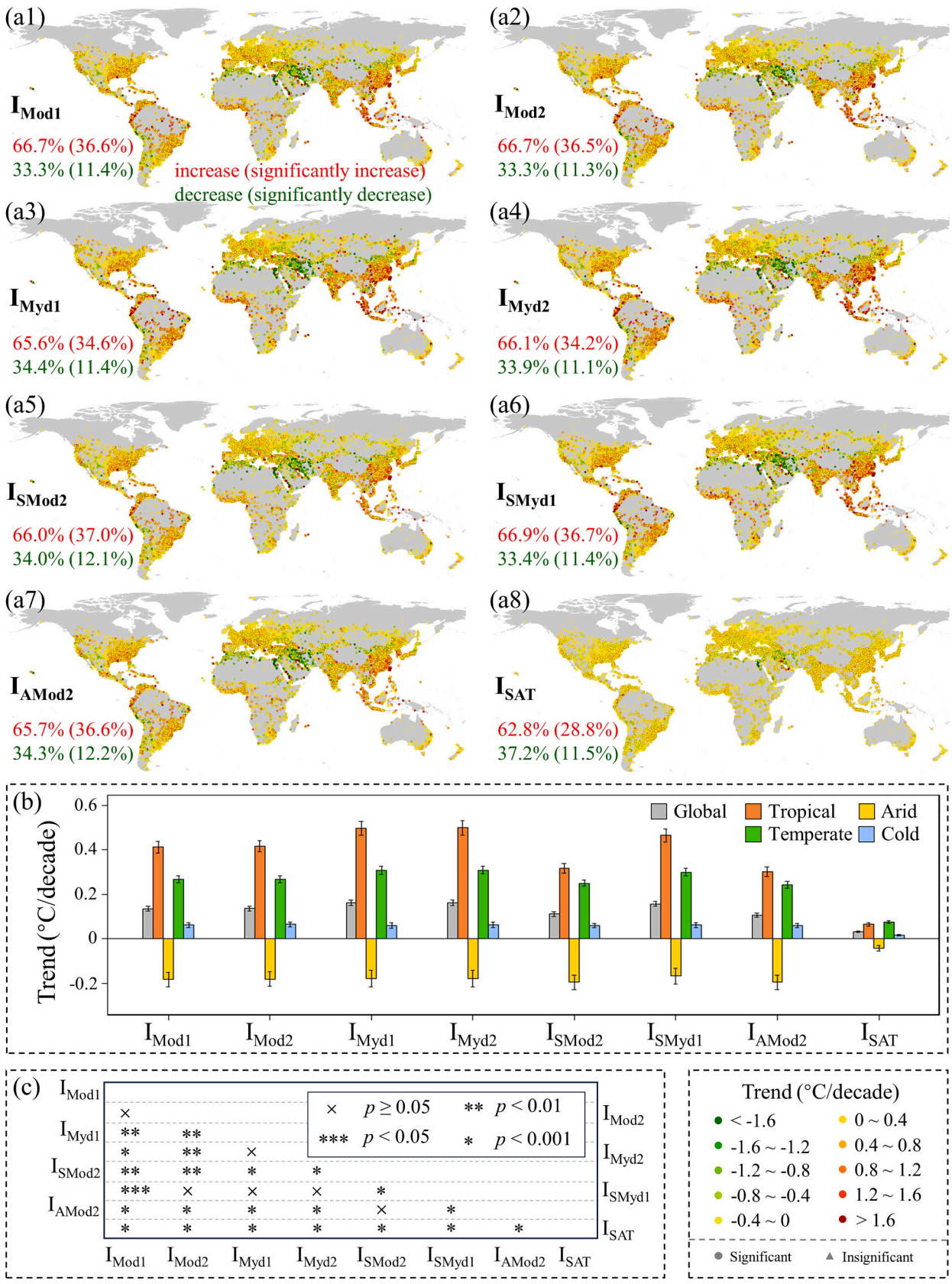

Fig. 7. Trends of annual daytime UHII derived from different temperature data. (a1-a8) Spatial patterns across global cities. (b) Mean values (95% confidence intervals) for different climate zones and for the globe. (c) Mutual comparisons through *t*-tests. The trend denotes the change rate of UHII estimated based on year-by-year values during 2003–2020. Please refer to Table 1 for specific details about each UHII indicator.

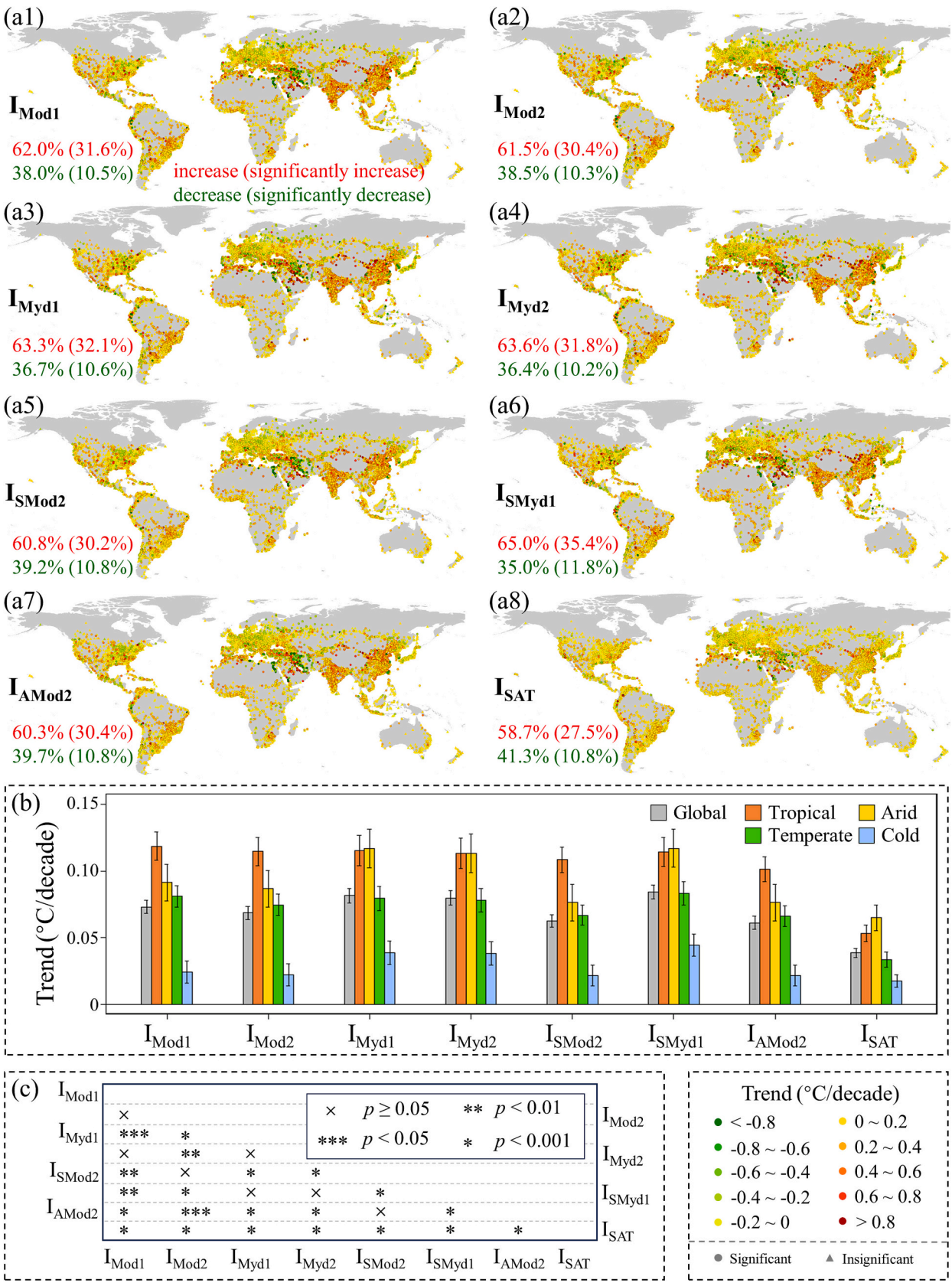

Fig. 8. Same as Fig. 7, but for annual nighttime UHII trends.

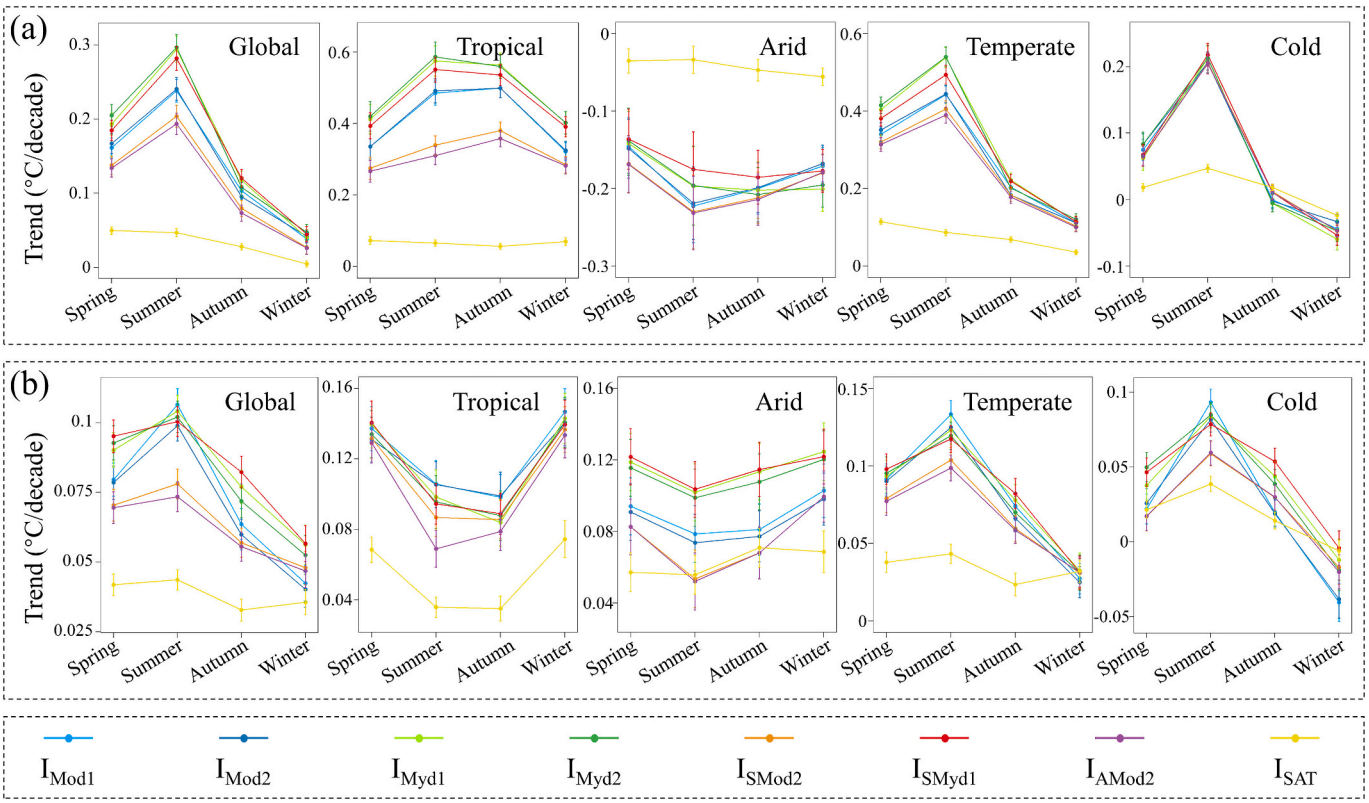

Fig. 9. Seasonal variations of the trend of UHII derived from different temperature data. (a) Daytime results. (b) Nighttime results. The trend denotes the change rate of UHII estimated based on year-by-year values during 2003–2020. Colored points and error bars represent the averages and 95% confidence intervals of UHII trends, respectively. Please refer to Table 1 for specific details about each UHII indicator.

outperforms the previous equal-area methods in mitigating anthropogenic interference (Fig. 3). As a result, it more effectively emphasizes the temperature difference between the urban area and its backgrounds (Tables 2–3).

(2) This study pioneers the development of a global, long-term, and multi-faceted UHII dataset.

In this study, we generate and provide a UHII dataset through the proposed DEA method, incorporating temperature data from various sources. Our UHII dataset has several advantages over previously published datasets. (a) Our UHII dataset spans a diverse range of regions and time periods, encompassing over 10,000 cities worldwide over a 20-year period on a monthly basis. (b) Our UHII dataset contains multi-faceted UHII indicators, including the regular clear-sky UHII based on the original MODIS LST, the all-sky UHII based on the seamless MODIS LST, and the canopy UHII derived from the gridded SAT. These advantages enable our UHII dataset to support various application scenarios. First, it facilitates the analysis of diurnal and seasonal patterns in the UHI effect. Recent studies have shown that clear-sky surface UHII exhibits a variety of complex diurnal and seasonal patterns influenced by factors such as evapotranspiration and surface albedo (Liu et al., 2022; Yang and Zhao, 2023). Our UHII dataset enables a more comprehensive analysis of diurnal and/or seasonal patterns of the UHI effect, encompassing comparative analyses of various UHII indicators (clear-sky and all-sky), assessment of the influence of city size and morphology, and examination of inter-annual trends. Second, our UHII dataset can be combined with advanced time-series analysis methods to explore the long-term dynamic characteristics of UHII. Currently, UHII and other urban climate trends are often estimated using linear regression methods (Chakraborty and Lee, 2019; Chakraborty and Qian, 2024; Du et al., 2023; Li et al., 2023; Yao et al., 2019; Yao et al., 2017), which overlooks the non-linear inter-annual variations of urban heat islands. Land transformation during urban expansion and extreme climatic conditions could lead to abrupt shifts in the UHI effect (Varentsova and Varentsov, 2021). Future studies could use time-series decomposition tools, such as Breaks For Additive Season and Trend (BFAST), to identify breakpoints in inter-annual UHII changes, thereby improving the detailed and accurate detection of long-term UHII trends. Third, our UHII dataset can be used to synergistically analyze factors influencing the UHI effect from both temporal and spatial perspectives. Peng et al. (2012) developed a multiple linear regression model of the clear-sky surface UHII using multi-year average data from 419 global cities, examining the primary drivers influencing the spatial distribution of the UHI effect. Yao et al. (2019) examined the inter-annual trends in clear-sky surface UHII from 2003 to 2019 across 397 major global cities, emphasizing that increased vegetation in rural areas contributes to intensifying the UHII effect. These studies have analyzed the drivers of the UHI effect from either a spatial or a temporal perspective. As the UHI is a spatiotemporal dynamic phenomenon, a simultaneous analysis combining both spatial and temporal dimensions can provide a more comprehensive understanding. Future research could employ dynamic space-time panel models (Debarsy et al., 2012) that integrate our UHII data with possible influencing factors (e.g., climate, landcover, and anthropogenic activities) to better understand the complex causes of the UHI effect. In summary, our UHII dataset represents a significant addition to the existing publicly available datasets, allowing researchers in efficiently conducting various UHI-related studies.

(3) This study systematically compares UHII estimates derived from different temperature data.

Temperature data serve as the foundation for quantifying the UHI phenomenon. Currently, most studies use the original MODIS LST data

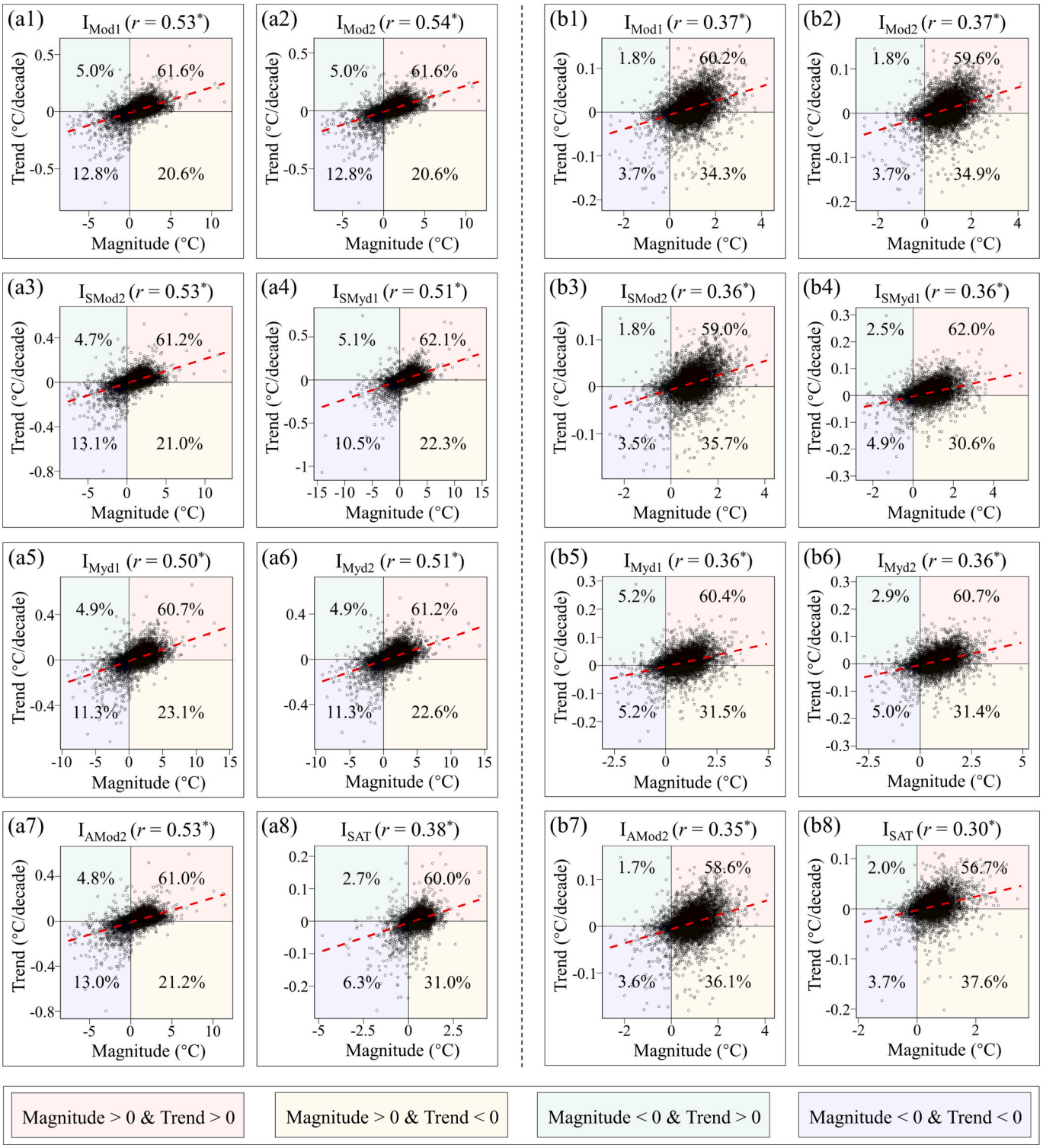

Fig. 10. Associations between the magnitude and trend of UHII. (a1-a8) Results for annual daytime UHII. (b1-b8) Results for annual nighttime UHII. The magnitude is calculated as the average of UHII during 2003–2020, while the trend denotes the change rate of UHII estimated based on year-by-year values during 2003–2020. Their relations are evaluated by Pearson correction coefficient (r) and significance (* $p < 0.05$). The numerical value within each quadrant denotes the percentage of cities falling within that quadrant. Subplots (a1-a8 or b1-b8) represent the results of eight UHII indicators derived from different temperature data and are detailed in Table 1.

for UHI analysis (Cao et al., 2016; Chakraborty and Lee, 2019; Li et al., 2022; Manoli et al., 2019; Mentaschi et al., 2022; Peng et al., 2012; Yang et al., 2017; Yang et al., 2019; Yang et al., 2023a; Yao et al., 2018a; Yao et al., 2017; Zhou et al., 2014; Zhou et al., 2015), while there are also several studies utilizing the gap-filled seamless MODIS LST or SAT for this purpose (Du et al., 2021; Du et al., 2023; Li and Chen, 2023; Liao et al., 2022; Yang and Zhao, 2023; Yang et al., 2023b; Yang et al., 2024). Despite potential differences in estimated UHII between different datasets, systematic comparative analyses are still lacking. This study addresses this gap by conducting a comprehensive analysis using our

multi-faceted UHII dataset. We find notable differences in the estimated UHII based on various temperature datasets. These differences arise not only between data types (LST or SAT) but also due to acquisition times (Terra or Aqua), weather conditions (clear-sky or all-sky), and processing methodologies (with or without gap filling). The discrepancies resulting from temperature data differences can influence several aspects of UHII, encompassing magnitudes, trends, and their spatial and temporal patterns. Notably, clear-sky surface UHII is found to be slightly (about a few to a dozen percent) higher than all-sky surface UHII and largely (up to several times) higher than canopy UHII, based on their global annual averages of magnitudes and trends (Tables 2–3). Additionally, the UHII estimated using the Terra LST tends to be lower than that using the Aqua LST, and the UHII estimated using the original LST data is typically higher than that estimated using the gap-filled seamless LST data (Tables 2–3). These results contribute to an objective assessment of the UHII effect, particularly indicating that the use of clear-sky observations may overestimate the actual UHII (more related to air temperature) perceived by people (Venter et al., 2021).

(4) This study investigates the magnitude and trend of UHII in a synergistic manner.

The magnitude and trend of UHII are pivotal aspects in the urban thermal environment research (Du et al., 2023; Manoli et al., 2019; Zhou et al., 2018). However, few studies have simultaneously analyzed both the magnitude and the trend of UHII on a global scale and explored their relationships. We conduct a synergistic analysis of the magnitude and trend of UHII using the dataset developed in this study. Our findings suggest that urbanization can induce localized temperature changes, manifesting as either localized temperature increases (heat islands) or decreases (cold islands) (Figs. 4–5). While the cold island phenomenon has been observed in several cities, predominantly in arid zones, the vast majority of global cities continue to face a heat island (Figs. 4–5). More importantly, our findings indicate a year-over-year increasing trend of UHII in most cities over this period (Figs. 7–8). Additionally, the trend of UHII is significantly and positively correlated with its magnitude (Fig. 10), indicating cities with stronger UHII tend to experience faster growth in UHII. This implies that cities with a more pronounced UHII may encounter elevated localized thermal risks in the future, emphasizing the urgency of improving the urban thermal environment. Previous studies have demonstrated that increasing green coverage, optimizing urban layout, and enhancing energy efficiency in buildings can effectively mitigate urban heat (Gago et al., 2013; Wong et al., 2021; Zhou et al., 2018). These measures not only contribute to alleviating the current urban heat issue but also yield positive long-term impacts on the city's future climate and environment.

5.2. Comparisons with previous research

Differences in data, methods, and time periods among previous studies have led to variations in the estimated UHII, even for the same city (Table S1). Taking Riyadh as an example, our results indicate that the annual daytime and nighttime canopy UHII are 0.15 °C and 1.86 °C, respectively (Fig. S1). These values are roughly consistent with the findings of Alghamdi and Moore (2015) but diverging greatly from those reported by Haddad et al. (2024). Taking Paris as another example, our results indicate that annual daytime surface UHII ranges from 1.58 °C to 2.63 °C, which is higher than the nighttime surface UHII, varying from 1.33 °C to 2.00 °C (Fig. S1). A similar day-night contrast was also observed by Chakraborty et al. (2019), but not in other studies (Le Roy et al., 2019; Sherafati et al., 2018). Obviously, the discrepancies between previous studies make it difficult to assess the reliability of our results by comparing them to a few specific cities. Fortunately, there are several global-scale studies analyzing the UHI effect, offering an opportunity to better validate the reliability of our results. The basic information and main quantitative results of the global UHI studies are presented in Tables S2-S3. Below, we will outline the main findings of these global studies and compare them with ours, focusing on the magnitude and trend of UHII, respectively.

Existing global-scale studies of magnitudes have focused primarily on surface UHII with a limited number of cities. For instance, Peng et al. (2012) quantified the surface UHII in 419 major global cities using the traditional equal-area (i.e. EA) method and discovered that the global average magnitude of surface UHII was 1.5 °C and 1.1 °C during the annual day and night, respectively. Li et al. (2022) estimated surface UHII in 1112 global cities using the modified equal-area (i.e. MEA) method and reported average magnitudes of 1.73 °C and 1.22 °C for annual daytime and nighttime, respectively. Du et al. (2021) conducted a simultaneous analysis of surface and canopy UHIIs in 336 global cities by using a distance-based method. They found that the global average magnitude of the annual daytime and nighttime surface UHIIs was 1.7 °C and 1.1 °C, respectively, surpassing the corresponding canopy UHIIs of 0.6 °C and 0.8 °C. The above studies are concentrated in major global cities, resulting in higher average magnitudes of UHII during both the annual day and night compared to our results averaged over 10,000 global cities (~1.2 °C and ~ 0.7 °C for surface UHII, ~0.46 °C and ~ 0.47 °C for canopy UHI, Table 2). This is primarily due to the general positive correlation between UHII and city size (Zhou et al., 2017). Thus, we categorized cities based on their sizes and calculated the average magnitude of UHII for each group (Fig. S2). When restricting the cities to those larger than 100 km^2 (totaling 930 cities), we found that the annually averaged magnitude of surface UHII was about 1.8 °C (day) and 1.2 °C (night), and canopy UHII was about 0.65 °C (day) and 0.73 °C (night) (Fig. S2). Obviously, these values are much closer to the annual averages of the above studies focused major global cities. Additionally, a global-scale analysis conducted by Chakraborty and Lee (2019) included over 7000 cities. This study reported global mean surface UHII magnitudes of 1.0 °C for annual daytime and 0.5 °C for annual nighttime, which are notably lower than those estimated by previous studies and ours. This could be attributed to the potential underestimation of UHII resulting from the simplified urban-extent (i.e. SUE) method they used, which selects the BRA in very close proximity to the urban area and does not account for reducing anthropogenic disturbance (Li et al., 2022; Yang et al., 2023b).

In terms of the UHII trends, a recent study by Du et al. (2023) analyzed the interannual trends of surface and canopy UHIIs over the period 2003–2020 in 5643 global cities. They showed that the surface UHII exhibited global average increasing trends of 0.19 °C/decade and 0.06 °C/decade during the annual day and night, respectively, while the canopy UHII exhibited global average increasing trends of about 0.03 °C/decade during both the annual day and night. The annual daytime and nighttime UHII trends estimated by Du et al. (2023) are somewhat in line with that calculated in our study (0.163 °C/decade and 0.080 °C/decade for surface UHII, 0.032 °C/decade and 0.039 °C/decade for canopy UHII, Table 3). Additionally, Yao et al. (2019) analyzed the interannual trend of surface UHII during 2003–2017 in 397 cities worldwide and reported global average increasing trends of 0.29 °C/decade and 0.10 °C/decade for annual daytime and nighttime, respectively. Given the general positive correlation between the UHII trend and city size (Fig. S3), the surface UHII trends identified by Yao et al. (2019) in 397 major global cities are notably higher than those averaged over 10,000 global cities in our study. However, upon focusing on the largest 397 cities within our dataset, we observed surface UHII trends of 0.222 °C/decade (daytime) and 0.095 °C/decade (nighttime) annually, which are only slightly lower than the results reported by Yao et al. (2019). The discrepancies between our results and previous studies are understandable due to differences in city samples and UHII estimation methods. It should be noted that Chakraborty and Lee (2019) and Si et al. (2022) also analyzed the surface UHII trends in global cities. However, the UHII trends obtained by them are notably weaker than those reported by other studies, possibly due to their use of the SUE method or its updated version, which may systematically underestimate

UHII (Li et al., 2022; Yang et al., 2023b).

In summary, while some disparities exist, our findings generally align with those of existing studies regarding the magnitude and trend of UHII. This, to some extent, supports the reliability of our datasets and results. It's crucial to note that previous studies have shown variations in data, methodology, and results, and have focused on solely one or two types of UHII (Tables S1-S2). This limits a comprehensive quantitative understanding of the UHII effect at global scales. Our study addresses this gap by examining eight different types of UHII in over 10,000 cities worldwide, using consistent data and methods. As such, it serves as a significant addition to the existing body of global UHII research.

5.3. Validations against other global UHII datasets

We compared our UHII dataset with two publicly available global surface UHII datasets. The first one, referred to here as the Chakraborty's dataset, covers 10,136 cities worldwide and was produced using the SUE method proposed by Chakraborty and Lee (2019). Apart from the city-level average surface UHII, the Chakraborty's dataset also includes spatially continuous pixel-level surface UHII in urban areas. We averaged these pixel-level surface UHII from the Chakraborty's dataset using our defined urban clusters, and then matched them to our surface UHII dataset based on the unique identifiers of the urban clusters. This approach overcomes the challenges of city-pair matching caused by discrepancies in the definition of city boundaries between our dataset and Chakraborty's dataset . For a fair comparison, we excluded cities without overlapping urban areas in both datasets and those with anomalous UHII values due to limited availability of pixel-level data. Ultimately, our comparative analyses included 7106 cities. Moreover, this comparative analysis was confined to using just 2020 data, owing to heavy workload constraints. As shown in Fig. 11, the surface UHII derived from our dataset shows a remarkable degree of congruence with that of Chakraborty's dataset. Despite the variations observed for individual cities, there is an evident linear correlation when considering the overall relationship between the two datasets (Fig. 11a). Besides, both datasets display a consistent distribution pattern of surface UHII across different climate zones (Fig. 11b). It is worth noting that the surface UHII estimated from the Chakraborty's dataset manifests a marked reduction compared to that estimated by our DEA method, while it approximates the surface UHII derived through the conventional EA method (Fig. 11b). This is because the SUE method used to generate the Chakraborty's dataset does not account for anthropogenic disturbance when estimating the UHII, resulting in a systematic bias towards lower UHII estimates (Li et al., 2022; Yang et al., 2023b). In addition to Chakraborty's dataset, we also included the summer 2013 surface UHII dataset published by CIESIN, which covers over 30,000 cities worldwide (Center for International Earth Science Information Network - CIESIN - Columbia University, 2016). However, due to variations in the location of cities and the boundaries of urban areas, it is challenging to perform city-by-city matching analyses. To overcome this, we selected the largest 10,196 cities (the same number as in our dataset) from the CIESIN dataset, and then compared the global and climate-zone mean surface UHIIs of these selected cities with those from our dataset. It is found that the surface UHII in the CIESIN dataset has average magnitudes similar to those obtained through the EA method, but noticeably lower than those estimated by our DEA method (Fig. S4). This is because the CIESIN dataset was generated using a traditional distance-based method, which simply defined the BRA as a 10 km buffer around the urban area, without considering the elimination of various confounding factors. However, the distribution pattern of the surface UHII in the CIESIN dataset is generally comparable to that of our dataset in terms of climate-zone averages (Fig. S4).

There is currently no publicly available canopy UHII dataset, which prevents us from performing a comparative analysis like the one as described above for surface UHII. To assess the reliability of our estimated canopy UHII, we have included another SAT data produced by Zhang et al. (2023), known as the HiTIC data. This data provides daily average SAT at 1 km resolution on a monthly basis, covering mainland

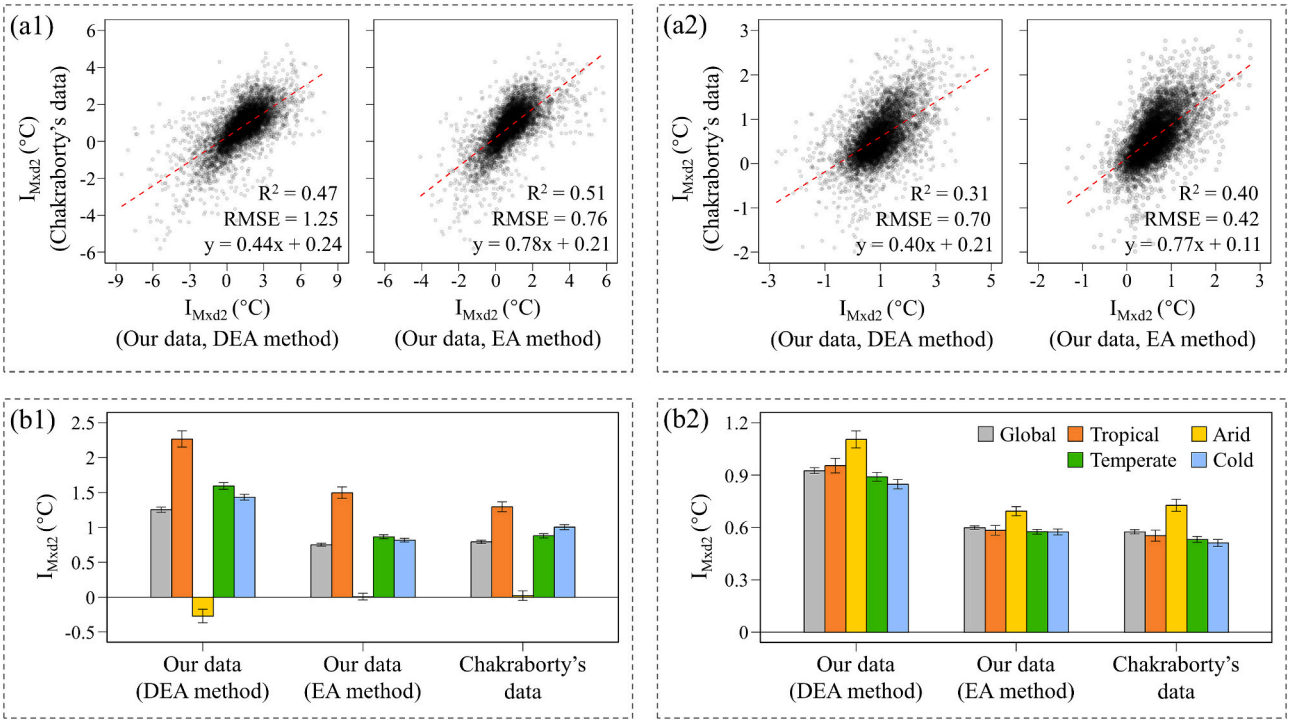

Fig. 11. Comparisons of surface UHII (I_{Mxd2}) between ours and that produced by Chakraborty and Lee (2019). (a1-b1) Annual daytime results during 2020. (a2-b2) Annual nighttime results during 2020. Columns and error bars in subplots (b1-b2) represent the averages and 95% confidence intervals, respectively. I_{Mxd2} refers to the average of I_{Mod2} and I_{Myd2}.The comparisons only include cities with partial or complete overlap of urban areas between our data and the Chakraborty's data, amounting to 7106 cities globally. Please refer to the Methods section for details about the EA and DEA methods.

China with high accuracy (RMSE = 0.60 °C). We applied the DEA method to the HiTIC SAT data and calculated the annual average canopy UHII for 1241 cities in mainland China in 2020. Subsequently, we compared these canopy UHII values with those from our own UHII dataset through city-to-city analysis. It is important to note that the HiTIC data only provides daily average SAT values for mainland China. Thus, to facilitate a fair comparison, we averaged our daytime and nighttime SATs, along with the corresponding canopy UHIIs, to represent their daily average values. The average SATs derived from the HiTIC SAT data show substantial agreement with the results of our study for both the urban area and the BRA (Fig. S5), confirming the reliability of the SAT data used in this analysis. In addition, the canopy UHII derived from the HiTIC SAT data shows a strong linear relationship and similar average magnitudes compared to our UHII dataset (Fig. S5).

In summary, although there are some discrepancies, our UHII dataset shows considerable overall consistency with existing datasets, partially confirming its credibility. Furthermore, it is noteworthy that existing data tend to underestimate the magnitude of UHII, highlighting the critical need to control for confounding factors, especially anthropogenic disturbance, when quantifying the UHI effect. This fact also underlines the advantages of our proposed DEA method.

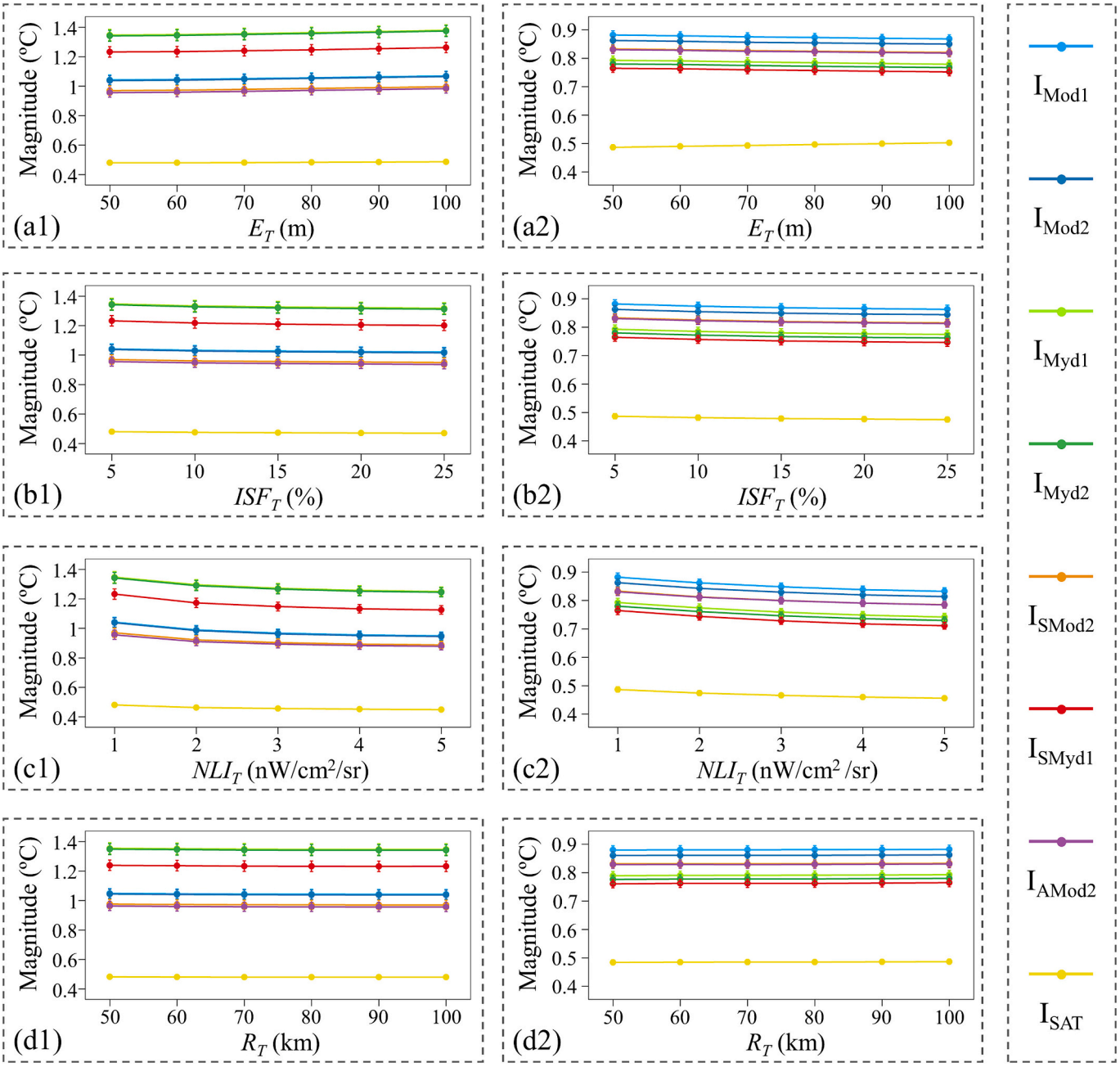

Fig. 12. Sensitivity of the global average magnitude of UHII to the parameters in the DEA method. (a1-a2) E_T denotes the upper threshold of the difference between the elevation of pixels within the background reference area (BRA) and the median elevation of the urban area. (b1-b2) ISF_T represents the upper threshold of impervious surface fraction for pixels within the BRA. (c1-c2) NLI_T represents the upper threshold of nighttime light intensity for pixels within the BRA. (d1-d2) R_T is the upper threshold for the buffer radius when searching for suitable pixels of the BRA. Those on the left (a1-d1) represent annual daytime results and those on the right (a2-d2) represent annual nighttime results. Colored points and error bars represent the averages and 95% confidence intervals, respectively. The sensitivity analysis is based on the estimated UHII using the DEA method for the year 2020. Please refer to Table 1 for detailed information regarding the eight UHII indicators.

5.4. Sensitivity analysis of the parameters in the DEA method

The DEA method mainly involves four parameters, including E_T, ISF_T, NLI_T, and R_T. E_T denotes the upper threshold for the difference between the elevation of pixels within the BRA and the median elevation of the urban area, utilized to mitigate the impact of topographic relief on UHII estimates. ISF_T and NLI_T represent the upper thresholds of ISF and NLI for pixels within the BRA, respectively, both aimed at mitigating the influence of anthropogenic disturbance on UHII estimates. R_T is the upper threshold for buffer radius, used to prevent the selection of BRA pixels located too far from the urban area. Referring to previous studies, we set E_T, ISF_T, NLI_T, and R_T to 50 m, 5%, 1 nW/cm^2/sr, and 100 km, respectively, as detailed in Section 3.1.2. To assess the sensitivity of UHII estimates to these parameters, we varied the value of each parameter and observed the resulting changes in UHII estimates over repeated experiments. During the sensitivity test for one parameter, all other parameters remained at their default values throughout the repeated experiments. Additionally, due to workload constraints, the parameter sensitivity analysis was limited to the year 2020. While there are year-to-year variations in the estimated UHII, these inter-annual differences are improbable to change the conclusions of parameter sensitivity analysis.

It is observed that the estimated UHII demonstrates an overall increasing trend with an increase in the E_T (Fig. 12a & Fig. S6a). Increasing E_T can lead to a greater elevation difference between the BRA and the urban area, especially notable in mountainous cities where surrounding elevations often largely surpass those of the urban area (Yang et al., 2023b). As temperature typically decreases with increasing elevation, the higher elevations in the BRA caused by larger E_T can lower its average temperature. Consequently, this reduction in temperature in the BRA can lead to an increase in the estimated UHII. Although alterations in E_T may affect cities with significant topographical variations (Yang et al., 2023b), their influence on global and regional UHII averages is minimal (Fig. 12a & Fig. S6a). For instance, increasing E_T from 50 m to 100 m results in less than a 2% change in the global mean UHII (Fig. 12a).

It is found that the increase in ISF_T or NLI_T generally results in a decrease in the estimated UHII (Fig. 12 & Fig. S6). Opting for larger values of ISF_T and NLI_T weakens the constraints on ISF and NLI within the BRA, potentially leading to an increase of these factors within the selected BRA. The magnitudes of ISF and NLI to some extent reflect the intensity of human activities, and they tend to be positively correlated with temperature (Li et al., 2019c; Yang et al., 2021). Therefore, an increase in ISF and/or NLI will result in a rise in the average temperature of the BRA and consequently a decrease in the estimated UHII. On average, globally, increasing ISF_T from the commonly used 5% to 25% results in a reduction in the estimated UHII of about 1–3% (Fig. 12b), while increasing NLI_T from 1 to 5 nW/cm^2/sr leads to a reduction in the estimated UHII of about 5–10% (Fig. 12c). Additionally, the estimated UHII demonstrates relatively higher sensitivity to NLI_T for tropical and arid cities (Fig. S6c). Therefore, imposing strict limits on ISF and NLI within the BRA is necessary to mitigate the impact of anthropogenic disturbance on UHII estimates. This rationale also underlies the decision to set ISF_T and NLI_T as relatively stricter thresholds in this study.

Compared to other parameters, changes in R_T have a much smaller overall effect on the estimated UHII (Fig. 12d & Fig. S6d). The R_T determines the maximum search extent when identifying the BRA. If the buffer radius reaches the R_T but does not capture enough valid BRA pixels, the selected BRA will be smaller than the urban area. When R_T is set to 100 km, <1% of cities experience a deficiency in selected BRA pixels. This proportion increases to 2% when R_T is reduced to 50 km. This suggests that over 98% of global cities are unaffected by changes in R_T. Consequently, the estimated UHII exhibits overall minimal sensitivity to R_T. Specifically, the transition from 50 km to 100 km in R_T results in less than a 1% change in both global and regional UHII averages (Fig. 12d & Fig. S6d).

Overall, although parameter variations can lead to changes in the estimated UHII, their effects are minimal and unlikely to alter the overall spatiotemporal patterns. This, to some extent, supports the robustness of our DEA method with respect to parameters. Although parameter changes have little effect on the estimated UHII on a global or regional scale, they may inevitably affect specific cities. Therefore, in this study, uniform and fixed parameters are used for all cities globally, reducing the uncertainty of varying parameters and improving comparability between cities.

5.5. Uncertainties in our UHII dataset

Our UHII dataset cannot fully capture the spatial and temporal details of the UHI effect. Firstly, it provides an overview of the temperature difference between urban areas and their BRAs, offering only a broad estimate of the UHII effect without capturing finer spatial variations. Complex urban landscapes and human activities can lead to heterogeneity in the spatial distribution of temperature within cities, creating localized areas of high and low temperatures (Yang et al., 2022; Yang et al., 2023c). Increasing green spaces and reducing industrial land use during urban renewal can lower localized temperature, helping to mitigate the UHI effect (Wang and Shu, 2020). Identifying small “cold islands” created by localized low-temperature areas in cities and understanding their spatial distribution and causes are crucial for improving the urban thermal environment (Kumar et al., 2024). Our UHII dataset lacks the ability to capture localized temperature changes, potentially overlooking the local benefits of mitigation measures during urban renewal. Second, our UHII dataset offers monthly data but lacks sufficient information on finer time scales, such as daily or weather-specific variations in UHII (Zhang et al., 2024). This limitation makes it challenging for our UHII dataset to capture dynamic changes in the urban thermal environment during short-term climate extremes, e.g. the interaction between the UHI effect and heat waves (Tian et al., 2023; Xue et al., 2023). Overall, our UHII dataset is well-suited for large-scale and long-term analyses of the UHI effect, but may introduce uncertainties when applied to localized or detailed analyses.

Our canopy UHII estimated by gridded SAT shows inconsistencies with that derived from in-situ observations. Most previous in-situ analyses have reported that the canopy UHII is generally higher at night than during the day (Alghamdi and Moore, 2015; Du et al., 2021; Le Roy et al., 2019; Venter et al., 2021; Wang et al., 2023). However, this diurnal pattern is not observed in our canopy UHII data for about half of the global cities. There may be two possible reasons for this discrepancy: (1) Differences between in-situ and gridded SATs. While global validation results indicate overall strong agreement between gridded SAT and in-situ observations (Yao et al., 2023), the estimated gridded SAT based on machine learning methods may be constrained by the input satellite-derived LST. This could potentially introduce a systematic bias in the estimated gridded SAT, influencing the resulting canopy UHII to exhibit patterns akin to surface UHII (e.g., higher values during daytime compared to nighttime). (2) Differences in the way UHII is calculated. Using spatially continuous gridded SAT data involves averaging SAT values across all pixels within urban areas or BRAs. In contrast, spatially dispersed in-situ observations calculate the mean SAT by averaging observations from all sites within these areas. This site sampling approach may not accurately reflect the overall average SAT of the urban area or the BRA, potentially introducing bias in the UHII calculated based on in-situ observations compared to gridded estimates.

To verify the above conjecture, we selected 30 Chinese cities, ensuring each city has at least one in-situ meteorological station within both its urban area and BRA (Fig. S7). The in-situ meteorological data were obtained from the China Meteorological Data Service Centre, which provides daily maximum (daytime) and minimum (nighttime) SATs for the year 2010. We calculated the annual average SAT of all in-situ observations within the urban area and the BRA separately (denoted as in-situ SAT), and then determined the canopy UHII (denoted as in-situ

I_{SAT}) for each city. Meanwhile, we extracted the gridded SATs for the pixels corresponding to in-situ stations and calculated the annual average values of these pixels within the urban area and the BRA separately (denoted as pixel-level SAT). We then calculated the difference in pixel-level SAT between the urban area and the BRA to obtain the canopy UHII (denoted as pixel-level I_{SAT}) for each city. The difference between pixel-level I_{SAT} and in-situ I_{SAT} reflects the impact of variations in SAT data on the estimated canopy UHII. Besides, we calculated the average gridded SAT of all available pixels within the urban area and the BRA separately (denoted as city-level SAT), and the obtained the canopy UHII (denoted as city-level I_{SAT}, i.e., the I_{SAT} obtained by our DEA method). The difference between city-level I_{SAT} and pixel-level I_{SAT} reflects the influence of UHII calculation ways on the estimated canopy UHII.

Our comparisons indicate that the pixel-level SAT is generally lower than the in-situ SAT, with the difference being more pronounced in the BRA than in the urban area (Fig. 13 and Fig. S8). This urban-rural asymmetry in the difference between pixel-level and in-situ SATs results in a higher pixel-level I_{SAT} compared to the in-situ I_{SAT} (Fig. 13 and Fig. S8). More importantly, the urban-rural asymmetry is more pronounced during the day, resulting in a greater overestimation of pixel-level I_{SAT} compared to in-situ I_{SAT} during daytime (Fig. 13 and Fig. S8). On average across the 30 Chinese cities, the annual daytime in-situ I_{SAT} is only 0.065 ± 0.130 °C, much smaller than the pixel-level I_{SAT} of 0.635 ± 0.143 °C (Fig. S8). Meanwhile, the annual nighttime in-situ I_{SAT} reaches 0.470 ± 0.218 °C, slightly smaller than the pixel-level I_{SAT} of 0.600 ± 0.135 °C (Fig. S8). Consequently, the pixel-level I_{SAT} does not exhibit the distinct nighttime-over-daytime characteristics observed in the in-situ I_{SAT}. Additionally, our comparisons indicate that, despite variations in some cities, the overall difference between city-level and pixel-level SATs does not show significant urban-rural asymmetry during both daytime and nighttime (Fig. 13 and Fig. S8). Consequently, the discrepancy between city-level I_{SAT} and pixel-level I_{SAT} is relatively small and shows minimal day-night variations (Fig. 13). On average for the 30 Chinese cities, the annual daytime city-level I_{SAT} is 0.610 ± 0.088 °C and the annual nighttime city-level I_{SAT} is 0.590 ± 0.099 °C, both of which are very close to the pixel-level I_{SAT} (Fig. S8). In general, the estimated canopy UHII can be influenced by both the data types (in-situ or gridded SAT) and the UHII calculation ways (pixel-level or city-level). However, the difference in SAT data seems to primarily account for the discrepancies between canopy UHIIs estimated by in-situ observations and gridded data. Compared to I_{SAT} estimated by in-situ observations, I_{SAT} derived from gridded data tends to overestimate daytime values, causing daytime I_{SAT} to approach or even exceed nighttime I_{SAT}.

To summarize, our UHII dataset presents some uncertainties due to limitations in the resolution and accuracy of available global temperature data. These uncertainties may limit the applicability of our UHII dataset, making it challenging to characterize detailed spatiotemporal patterns of UHII within a city and potentially leading to an overestimation of daytime canopy UHII in some cities. Future work should focus on urban areas and their surroundings, developing large-scale, multi-source, high-resolution temperature products capable of accurately depicting complex urban-rural scenarios for global cities. This effort is crucial for enhancing the reliability of UHII quantitative results and gaining detailed knowledge of the spatiotemporal patterns in the urban thermal environment.

5.6. *Limitations and future work*

First, we utilize the MODIS landcover product to delineate the urban extent. Different globally available urban extent products show differences in the delineation of urban areas, and the choice of different products also affects the measured UHII (Yang et al., 2023a). However, a

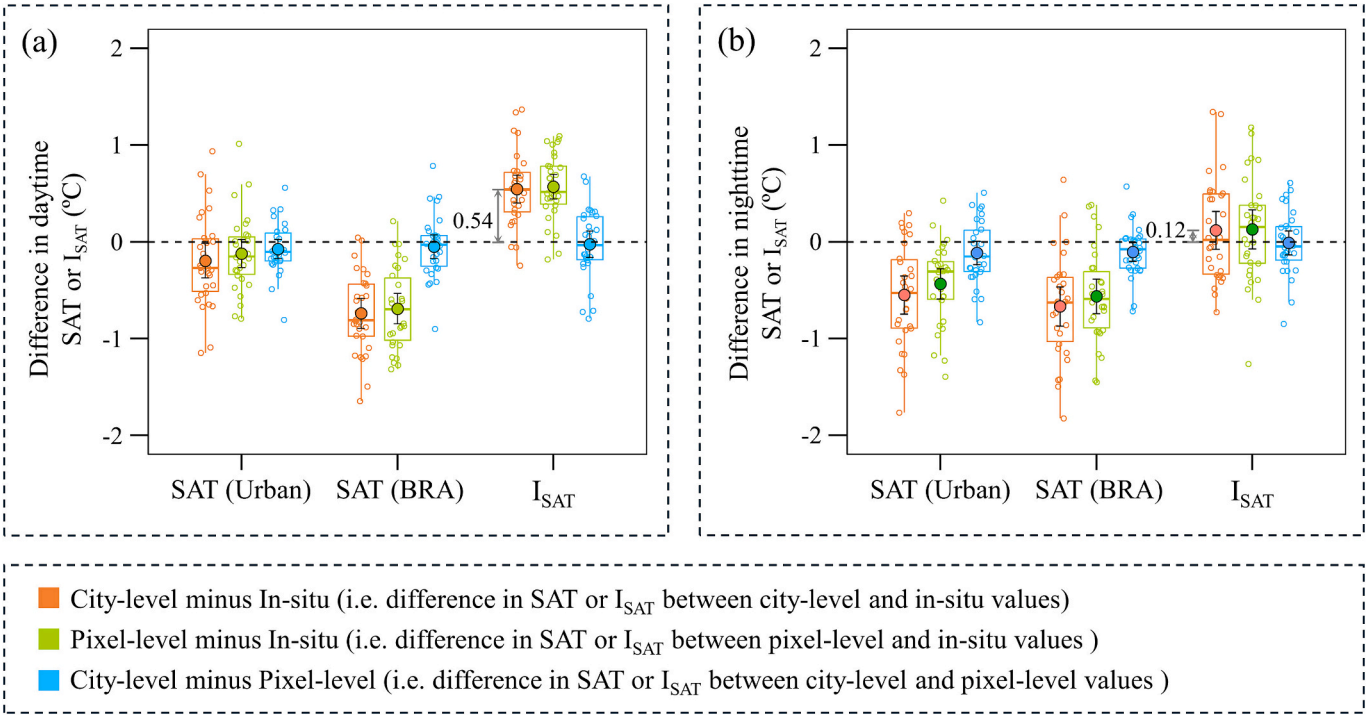

Fig. 13. Differences in surface air temperature (SAT) and canopy UHII (I_{SAT}) between those derived from the in-situ observations and those derived from gridded data across 30 Chinese cities. The in-situ SAT is derived from the China Meteorological Data Centre, and the pixel-level or city-level SAT is extracted from the gridded data provided by Yao et al. (2023). The pixel-level SAT refers to the average gridded SAT of pixels at the locations of in-situ meteorological stations within the urban area or the background reference area (BRA). The city-level SAT refers to the average gridded SAT for all available pixels within the urban area or the BRA. The central lines in the boxes are the median values. The color-filled dots in the boxes and the error bars around them show the mean and 95% confidence intervals. The locations of the 30 Chinese cities are presented in Fig. S7 in the supplementary materials.

lack of consensus on the classification of urban areas complicates the selection of an optimal urban extent product (Li et al., 2020; Taubenböck et al., 2019; Zhao et al., 2022). Moreover, the MODIS LST products, and thus all the datasets derived from these products, use a classification-based emissivity approach that is constrained by this MODIS land cover (Snyder et al., 1998). Therefore, to maintain internal consistency between LST and land cover, we use only the MODIS product for delineating urban extents in this study.

Second, this study proposes a new DEA method and demonstrates its effectiveness in estimating UHII by comparing it with existing area-based methods. However, various recent methods for quantifying UHII have been proposed, such as the SUE method (Chakraborty and Lee, 2019), the ISF-based method (Li et al., 2018b), and the adaptive synchronous extraction (ASE) method (Yang et al., 2023b). The advantages, disadvantages, and applicable scenarios of these methods have been extensively discussed in previous studies (Yang et al., 2023a; Yang et al., 2023b). For instance, the ISF-based method gets rid of the delineation of urban and rural areas, but the assumed linear relationship between ISF and LST by this method is not universally satisfied for all cities (Yang et al., 2023a). The SUE method is favored for its simplicity, but it is constrained by systematically lower UHII due to the BRA often being too close to the urban area (Li et al., 2022; Yang et al., 2023b). Moreover, the ASE method demonstrates the ability to select the most optimal BRA, but its complexity often requires considerable computing power for large-scale applications (Yang et al., 2023b). As these methods have been extensively compared in previous studies, they are not considered again in this analysis. Instead, the focus of this study is on comparing area-based methods that are more directly relevant to our proposed DEA method and then developing the global UHII dataset.

Third, this study integrates temperature data from eight different sources to create a multi-faceted UHII dataset. Although we also have calculated canopy UHII from one gridded estimate of SAT, other thermal metrics (e.g., heat index, humidex, wet-bulb temperature, dew point temperature), more pertinent to human perception (Chakraborty et al., 2022; Wang et al., 2023), are still absent. We intend to expand our UHII dataset in the future, particularly as global high-resolution data with additional thermal metrics become available.

6. Conclusion

Publicly released UHII datasets are relatively few and have the following limitations: (1) a focus on clear-sky surface UHII, lack of datasets for all-sky surface UHII and canopy UHII; (2) the estimation methods used often neglect the impact of anthropogenic interference, resulting in uncertainties in the estimated UHII. To address the above issues, this study proposes a new DEA method for UHII estimation. We apply this method to eight different gridded temperature datasets to create a long-term, multi-faceted UHII dataset covering over 10,000 cities worldwide. Based on this dataset, we conduct a comprehensive analysis of the magnitude and trend of UHII obtained by different methods and temperature datasets.

The DEA method proposed in this study effectively mitigates the influence of various confounding factors, including water bodies, topography relief, and anthropogenic disturbance, on the selection of the BRA. More importantly, the DEA method ensures that the size of selected BRA is sufficient (equal to the urban area) and can reflect the background climate (not too far away from the urban area). Quantitative comparison results indicate that, in contrast to existing area-based methods, the DEA method is more adept at mitigating the influence of anthropogenic disturbance. Besides, the UHII estimated by the DEA method exhibits higher magnitude and trend, indicating its efficacy in emphasizing the impact of urbanization on local temperature.

Over 80% of global cities experience UHII greater than zero, and over 60% of global cities witness an upward interannual trend in UHII over the past two decades. The global average magnitudes of surface UHII are approximately 1 °C (0.881–1.239 °C, depending on the temperature data source) and 0.8 °C (0.708–0.832 °C) during the day and night, respectively, throughout the year, which are significantly higher than the magnitudes of canopy UHII for both the annual daytime average (0.457 °C) and the annual nighttime average (0.473 °C). The global average trends of surface UHII exceed 0.1 °C/decade (0.106–0.163 °C/decade) and 0.06 °C/decade (0.061–0.082 °C/decade) during the day and night, respectively, throughout the year, which are much stronger than the trends of canopy UHII for both the annual daytime average (0.032 °C/decade) and the annual nighttime average (0.039 °C/decade). Notably, there exists a positive correlation between the magnitude and trend of UHII, indicating that cities with stronger UHII tend to experience faster growth in UHII. This reinforcing cycle between UHII and its trend emphasizes the urgent need for immediate action in managing urban thermal environments.

Differences in UHII based on various temperature datasets are notable. These differences arise not only between data types (LST or SAT) but also due to acquisition times (Terra or Aqua), weather conditions (clear-sky or all-sky), and processing methodologies (with or without gap filling). The findings reveal that clear-sky surface UHII tends to be marginally higher (about a few to a dozen percent) than all-sky surface UHII, and substantially higher (up to several times) than canopy UHII, both in magnitudes and trends. Additionally, the UHII estimated from the Terra LST tends to be lower compared to estimates from the Aqua LST, while UHII calculated from the original LST data generally exceeds that derived from the gap-filled seamless LST data. Therefore, carefully choosing appropriate temperature data and combining various UHII indicators are crucial for gaining a thorough and accurate understanding of the urban thermal environment.

In summary, the main contributions of this study can be summarized as follows. (1) We introduce a new DEA method that demonstrates superior effectiveness in mitigating the influence of confounding factors on UHII estimates. (2) We develop a global, long-term, multi-faceted UHII dataset, which addresses the gap in publicly available all-sky surface or canopy UHII datasets. (3) We identify positive correlations between the magnitude and trend of UHII, and provide a systematic comparison results of UHII estimates derived from different temperature data sources. Overall, our proposed DEA method and UHII dataset, as well as the analysis results, are expected to draw the attention of the research community towards advancing research on the urban thermal environment.

CRediT authorship contribution statement

Qiquan Yang: Writing – review & editing, Writing – original draft, Visualization, Software, Resources, Methodology, Investigation, Funding acquisition, Conceptualization. **Yi Xu:** Writing – review & editing, Supervision, Funding acquisition. **TC Chakraborty:** Writing – review & editing, Formal analysis. **Meng Du:** Visualization, Formal analysis, Data curation. **Ting Hu:** Writing – review & editing, Software. **Yue Liu:** Writing – review & editing, Resources, Investigation. **Rui Yao:** Writing – review & editing, Resources. **Jie Yang:** Writing – review & editing, Resources. **Shurui Chen:** Writing – review & editing, Visualization. **Changjiang Xiao:** Writing – review & editing, Visualization. **Renrui Liu:** Writing – review & editing, Visualization. **Mingjie Zhang:** Writing – review & editing, Visualization, Resources. **Rui Chen:** Writing – review & editing.

Declaration of competing interest

The authors declare that they have no known competing financial interests or personal relationships that could have appeared to influence the work reported in this paper.

Data availability

The global NPP-VIIRS-like nighttime light intensity data is available

at https://doi.org/10.7910/DVN/YGIVCD. The global impervious surface area data is available from http://irsip.whu.edu.cn/resources/resources_v2.php. The Köppen-Geiger Climate Classification global map is available from https://www.gloh2o.org/koppen/. The global seamless gridded temperature datasets are available from https://cjgeodata.cug.edu.cn/#/pageDetail?id=97 and https://doi.org/10.25380/iastate.c.5078492.v3. All the other data can be accessed from the Google Earth Engine platform (https://code.earthengine.google.com/). All data are available upon reasonable request from the authors.

Acknowledgments

This research was supported by the Macau Young Scholars Program (AM2022001), the National Natural Science Foundation of China (42201389), the Science and Technology Development Fund of Macau (0014/2022/A1 and 0005/2020/A1), and the Postdoctoral Science Foundation of China (2021TQ0245, 2021M702470, and 2023M730735). T.C.'s contribution was supported by a U.S. Department of Energy Office of Science Early Career grant. PNNL is operated for the Department of Energy by Battelle Memorial Institute under contract DE-AC05-76RL01830.

Appendix A. Supplementary data

Supplementary data to this article can be found online at https://doi.org/10.1016/j.rse.2024.114343.

References

Alghamdi, A.S., Moore, T.W., 2015. Detecting temporal changes in Riyadh's urban heat island. Pap. Appl. Geogr. 1, 312–325.
Beck, H.E., Zimmermann, N.E., McVicar, T.R., Vergopolan, N., Berg, A., Wood, E.F., 2018. Present and future Köppen-Geiger climate classification maps at 1-km resolution. Sci. Data 5, 1–12.
Cai, Z., La Sorte, F.A., Chen, Y., Wu, J., 2023. The surface urban heat island effect decreases bird diversity in Chinese cities. Sci. Total Environ. 902, 166200.
Cao, C., Lee, X., Liu, S., Schultz, N., Xiao, W., Zhang, M., Zhao, L., 2016. Urban heat islands in China enhanced by haze pollution. Nat. Commun. 7, 12509.
Center for International Earth Science Information Network - CIESIN - Columbia University, 2016. Global Urban Heat Island (UHI) Data Set, 2013. Palisades, New York. NASA Socioeconomic Data and Applications Center (SEDAC).
Chakraborty, T., Lee, X., 2019. A simplified urban-extent algorithm to characterize surface urban heat islands on a global scale and examine vegetation control on their spatiotemporal variability. Int. J. Appl. Earth Obs. Geoinf. 74, 269–280.
Chakraborty, T.C., Qian, Y., 2024. Urbanization exacerbates continental-to regional-scale warming. One Earth 2590–3330.
Chakraborty, T., Hsu, A., Manya, D., Sheriff, G., 2019. Disproportionately higher exposure to urban heat in lower-income neighborhoods: a multi-city perspective. Environ. Res. Lett. 14, 105003.
Chakraborty, T., Hsu, A., Manya, D., Sheriff, G., 2020. A spatially explicit surface urban heat island database for the United States: characterization, uncertainties, and possible applications. ISPRS J. Photogramm. Remote Sens. 168, 74–88.
Chakraborty, T., Lee, X., Ermida, S., Zhan, W., 2021a. On the land emissivity assumption and landsat-derived surface urban heat islands: a global analysis. Remote Sens. Environ. 265, 112682.
Chakraborty, T., Sarangi, C., Lee, X., 2021b. Reduction in human activity can enhance the urban heat island: insights from the COVID-19 lockdown. Environ. Res. Lett. 16, 054060.
Chakraborty, T., Venter, Z., Qian, Y., Lee, X., 2022. Lower urban humidity moderates outdoor heat stress. AGU Adv. 3, e2022AV000729.
Chakraborty, T., Newman, A.J., Qian, Y., Hsu, A., Sheriff, G., 2023. Residential segregation and outdoor urban moist heat stress disparities in the United States. One Earth 6, 738–750.
Chen, Z., Yu, B., Yang, C., Zhou, Y., Yao, S., Qian, X., Wang, C., Wu, B., Wu, J., 2021. An extended time series (2000–2018) of global NPP-VIIRS-like nighttime light data from a cross-sensor calibration. Earth Syst. Sci. Data 13, 889–906.
Chen, S., Yang, Y., Deng, F., Zhang, Y., Liu, D., Liu, C., Gao, Z., 2022. A high-resolution monitoring approach of canopy urban heat island using a random forest model and multi-platform observations. Atmos. Meas. Tech. 15, 735–756.
Chen, Q., Liu, R., Cheng, Q., Chen, Y., Cao, S., Du, M., Li, K., 2023. Evaluating the impact of sky view factor and building shadow ratio on air temperature in different residential and commercial building scenarios: a case study of Beijing, China. Urban Clim. 49, 101509.
Clinton, N., Gong, P., 2013. MODIS detected surface urban heat islands and sinks: global locations and controls. Remote Sens. Environ. 134, 294–304.
Debarsy, N., Ertur, C., LeSage, J.P., 2012. Interpreting dynamic space–time panel data models. Stat. Methodol. 9, 158–171.
Devereux, D., Caccetta, P., 2019. Land Surface Temperature and Urban Heat Island Estimates for Australian Capital Cities, Summer 2018-19. Australia. Commonwealth Scientific and Industrial Research Organisation (CSIRO).
Du, H., Wang, D., Wang, Y., Zhao, X., Qin, F., Jiang, H., Cai, Y., 2016. Influences of land cover types, meteorological conditions, anthropogenic heat and urban area on surface urban heat island in the Yangtze River Delta urban agglomeration. Sci. Total Environ. 571, 461–470.
Du, H., Zhan, W., Liu, Z., Li, J., Li, L., Lai, J., Miao, S., Huang, F., Wang, C., Wang, C., 2021. Simultaneous investigation of surface and canopy urban heat islands over global cities. ISPRS J. Photogramm. Remote Sens. 181, 67–83.
Du, H., Zhan, W., Voogt, J., Bechtel, B., Chakraborty, T.C., Liu, Z., Hu, L., Wang, Z., Li, J., Fu, P., 2023. Contrasting trends and drivers of global surface and canopy urban heat islands. Geophys. Res. Lett. 50, e2023GL104661.
Gago, E.J., Roldan, J., Pacheco-Torres, R., Ordóñez, J., 2013. The city and urban heat islands: a review of strategies to mitigate adverse effects. Renew. Sust. Energ. Rev. 25, 749–758.
Gui, X., Wang, L., Yao, R., Yu, D., Li, C.a., 2019. Investigating the urbanization process and its impact on vegetation change and urban heat island in Wuhan, China. Environ. Sci. Pollut. Res. 26, 30808–30825.
Haddad, S., Zhang, W., Paolini, R., Gao, K., Altheeb, M., Al Mogirah, A., Bin Moammar, A., Hong, T., Khan, A., Cartalis, C., 2024. Quantifying the energy impact of heat mitigation technologies at the urban scale. Nat. Cities 1, 62–72.
Hong, F., Zhan, W., Göttsche, F.-M., Liu, Z., Dong, P., Fu, H., Huang, F., Zhang, X., 2022. A global dataset of spatiotemporally seamless daily mean land surface temperatures: generation, validation, and analysis. Earth Syst. Sci. Data 14, 3091–3113.
Hsu, A., Sheriff, G., Chakraborty, T., Manya, D., 2021. Disproportionate exposure to urban heat island intensity across major US cities. Nat. Commun. 12, 2721.
Huang, X., Song, Y., Yang, J., Wang, W., Ren, H., Dong, M., Feng, Y., Yin, H., Li, J., 2022. Toward accurate mapping of 30-m time-series global impervious surface area (GISA). Int. J. Appl. Earth Obs. Geoinf. 109, 102787.
Imhoff, M.L., Zhang, P., Wolfe, R.E., Bounoua, L., 2010. Remote sensing of the urban heat island effect across biomes in the continental USA. Remote Sens. Environ. 114, 504–513.
Jia, A., Liang, S., Wang, D., Ma, L., Wang, Z., Xu, S., 2023. Global hourly, 5 km, all-sky land surface temperature data from 2011 to 2021 based on integrating geostationary and polar-orbiting satellite data. Earth Syst. Sci. Data 15, 869–895.
Kumar, P., Debele, S.E., Khalili, S., Halios, C.H., Sahani, J., Aghamohammadi, N., de Fatima Andrade, M., Athanassiadou, M., Bhui, K., Calvillo, N., 2024. Urban heat mitigation by green and blue infrastructure: drivers, effectiveness, and future needs. Innovation 5, 100588.
Lai, J., Zhan, W., Huang, F., Voogt, J., Bechtel, B., Allen, M., Peng, S., Hong, F., Liu, Y., Du, P., 2018. Identification of typical diurnal patterns for clear-sky climatology of surface urban heat islands. Remote Sens. Environ. 217, 203–220.
Le Roy, B., Lemonsu, A., Kounkoud-arnaud, R., Brion, D., Masson, V., 2019. Long time series spatialized data for urban climatological studies: a case study of Paris, France. Int. J. Climatol. 40, 3567–3584.
Levin, N., Kyba, C.C., Zhang, Q., de Miguel, A.S., Román, M.O., Li, X., Portnov, B.A., Molthan, A.L., Jechow, A., Miller, S.D., 2020. Remote sensing of night lights: a review and an outlook for the future. Remote Sens. Environ. 237, 111443.
Li, K., Chen, Y., 2023. Characterizing the indicator-based, day-and-night, and climate-based variations in response of surface urban heat island during heat wave across global 561 cities. Sustain. Cities Soc. 99, 104877.
Li, H., Meier, F., Lee, X., Chakraborty, T., Liu, J., Schaap, M., Sodoudi, S., 2018a. Interaction between urban heat island and urban pollution island during summer in Berlin. Sci. Total Environ. 636, 818–828.
Li, H., Zhou, Y., Li, X., Meng, L., Wang, X., Wu, S., Sodoudi, S., 2018b. A new method to quantify surface urban heat island intensity. Sci. Total Environ. 624, 262–272.
Li, D., Liao, W., Rigden, A.J., Liu, X., Wang, D., Malyshev, S., Shevliakova, E., 2019a. Urban heat island: aerodynamics or imperviousness? Sci. Adv. 5, eaau4299.
Li, K., Chen, Y., Wang, M., Gong, A., 2019b. Spatial-temporal variations of surface urban heat island intensity induced by different definitions of rural extents in China. Sci. Total Environ. 669, 229–247.
Li, L., Yu, T., Zhao, L., Zhan, Y., Zheng, F., Zhang, Y., Mumtaz, F., Wang, C., 2019c. Characteristics and trend analysis of the relationship between land surface temperature and nighttime light intensity levels over China. Infrared Phys. Technol. 97, 381–390.
Li, X., Zhou, Y., Yu, S., Jia, G., Li, H., Li, W., 2019d. Urban heat island impacts on building energy consumption: a review of approaches and findings. Energy 174, 407–419.
Li, X., Gong, P., Zhou, Y., Wang, J., Bai, Y., Chen, B., Hu, T., Xiao, Y., Xu, B., Yang, J., 2020. Mapping global urban boundaries from the global artificial impervious area (GAIA) data. Environ. Res. Lett. 15, 094044.
Li, K., Chen, Y., Gao, S., 2022. Uncertainty of city-based urban heat island intensity across 1112 global cities: background reference and cloud coverage. Remote Sens. Environ. 271, 112898.
Li, L., Zhan, W., Hu, L., Chakraborty, T., Wang, Z., Fu, P., Wang, D., Liao, W., Huang, F., Fu, H., 2023. Divergent urbanization-induced impacts on global surface urban heat island trends since 1980s. Remote Sens. Environ. 295, 113650.
Liao, Y., Shen, X., Zhou, J., Ma, J., Zhang, X., Tang, W., Chen, Y., Ding, L., Wang, Z., 2022. Surface urban heat island detected by all-weather satellite land surface temperature. Sci. Total Environ. 811, 151405.
Liu, H., Huang, B., Zhan, Q., Gao, S., Li, R., Fan, Z., 2021. The influence of urban form on surface urban heat island and its planning implications: evidence from 1288 urban clusters in China. Sustain. Cities Soc. 71, 102987.

Liu, Z., Zhan, W., Lai, J., Bechtel, B., Lee, X., Hong, F., Li, L., Huang, F., Li, J., 2022. Taxonomy of seasonal and diurnal clear-sky climatology of surface urban heat island dynamics across global cities. ISPRS J. Photogramm. Remote Sens. 187, 14–33.
Liu, H., He, B.-J., Gao, S., Zhan, Q., Yang, C., 2023. Influence of non-urban reference delineation on trend estimate of surface urban heat island intensity: a comparison of seven methods. Remote Sens. Environ. 296, 113735.
Luo, M., Lau, N.C., 2018. Increasing heat stress in urban areas of eastern China: acceleration by urbanization. Geophys. Res. Lett. 45, 13060–13069.
Manoli, G., Fatichi, S., Schläpfer, M., Yu, K., Crowther, T.W., Meili, N., Burlando, P., Katul, G.G., Bou-Zeid, E., 2019. Magnitude of urban heat islands largely explained by climate and population. Nature 573, 55–60.
Manoli, G., Fatichi, S., Bou-Zeid, E., Katul, G.G., 2020. Seasonal hysteresis of surface urban heat islands. Proc. Natl. Acad. Sci. 117, 7082–7089.
Mentaschi, L., Duveiller, G., Zulian, G., Corbane, C., Pesaresi, M., Maes, J., Stocchino, A., Feyen, L., 2022. Global long-term mapping of surface temperature shows intensified intra-city urban heat island extremes. Glob. Environ. Chang. 72, 102441.
Mo, Y., Xu, Y., Chen, H., Zhu, S., 2021. A review of reconstructing remotely sensed land surface temperature under cloudy conditions. Remote Sens. 13, 2838.
Niu, L., Peng, Z., Tang, R., Zhang, Z., 2021. Development of a long-term dataset of China surface urban heat island for policy making: spatio-temporal characteristics. In: 2021 IEEE International Geoscience and Remote Sensing Symposium IGARSS. IEEE, pp. 6928–6931.
Peng, S., Piao, S., Ciais, P., Friedlingstein, P., Ottle, C., Bréon, F.-M., Nan, H., Zhou, L., Myneni, R.B., 2012. Surface urban heat island across 419 global big cities. Environ. Sci. Technol. 46, 696–703.
Ren, Y., Lafortezza, R., Giannico, V., Sanesi, G., Zhang, X., Xu, C., 2023. The unrelenting global expansion of the urban heat island over the last century. Sci. Total Environ. 880, 163276.
Rizwan, A.M., Dennis, L.Y., Chunho, L., 2008. A review on the generation, determination and mitigation of urban Heat Island. J. Environ. Sci. 20, 120–128.
Shao, L., Liao, W., Li, P., Luo, M., Xiong, X., Liu, X., 2023. Drivers of global surface urban heat islands: surface property, climate background, and 2D/3D urban morphologies. Build. Environ. 242, 110581.
Sherafati, S., Saradjian, M.R., Rabbani, A., 2018. Assessment of surface urban heat island in three cities surrounded by different types of land-cover using satellite images. J. Indian Soc. Remote Sens. 46, 1013–1022.
Si, M., Li, Z.-L., Nerry, F., Tang, B.-H., Leng, P., Wu, H., Zhang, X., Shang, G., 2022. Spatiotemporal pattern and long-term trend of global surface urban heat islands characterized by dynamic urban-extent method and MODIS data. ISPRS J. Photogramm. Remote Sens. 183, 321–335.
Snyder, W.C., Wan, Z., Zhang, Y., Feng, Y.-Z., 1998. Classification-based emissivity for land surface temperature measurement from space. Int. J. Remote Sens. 19, 2753–2774.
Taubenböck, H., Weigand, M., Esch, T., Staab, J., Wurm, M., Mast, J., Dech, S., 2019. A new ranking of the world's largest cities—do administrative units obscure morphological realities? Remote Sens. Environ. 232, 111353.
Tian, W., Yang, Y., Wang, L., Zong, L., Zhang, Y., Liu, D., 2023. Role of local climate zones and urban ventilation in canopy urban heat island–heatwave interaction in Nanjing megacity, China. Urban Clim. 49, 101474.
Varentsova, S.A., Varentsov, M.I., 2021. A new approach to study the long-term urban heat island evolution using time-dependent spectroscopy. Urban Clim. 40, 101026.
Venter, Z.S., Chakraborty, T., Lee, X., 2021. Crowdsourced air temperatures contrast satellite measures of the urban heat island and its mechanisms. Sci. Adv. 7, eabb9569.
Wang, W., Shu, J., 2020. Urban renewal can mitigate urban heat islands. Geophys. Res. Lett. 47, e2019GL085948.
Wang, C., Zhan, W., Li, L., Wang, S., Wang, C., Miao, S., Du, H., Jiang, L., Jiang, S., 2023. Urban heat islands characterized by six thermal indicators. Build. Environ. 244, 110820.
Wong, N.H., Tan, C.L., Kolokotsa, D.D., Takebayashi, H., 2021. Greenery as a mitigation and adaptation strategy to urban heat. Nat. Rev. Earth Environ. 2, 166–181.
Xue, J., Zong, L., Yang, Y., Bi, X., Zhang, Y., Zhao, M., 2023. Diurnal and interannual variations of canopy urban heat island (CUHI) effects over a mountain–valley city with a semi-arid climate. Urban Clim. 48, 101425.
Yang, C., Zhao, S., 2023. Diverse seasonal hysteresis of surface urban heat islands across Chinese cities: patterns and drivers. Remote Sens. Environ. 294, 113644.
Yang, Q., Huang, X., Li, J., 2017. Assessing the relationship between surface urban heat islands and landscape patterns across climatic zones in China. Sci. Rep. 7, 9337.
Yang, Q., Huang, X., Tang, Q., 2019. The footprint of urban heat island effect in 302 Chinese cities: temporal trends and associated factors. Sci. Total Environ. 655, 652–662.
Yang, Q., Huang, X., Yang, J., Liu, Y., 2021. The relationship between land surface temperature and artificial impervious surface fraction in 682 global cities: spatiotemporal variations and drivers. Environ. Res. Lett. 16, 024032.
Yang, Y., Guo, M., Ren, G., Liu, S., Zong, L., Zhang, Y., Zheng, Z., Miao, Y., Zhang, Y., 2022. Modulation of wintertime canopy urban Heat Island (CUHI) intensity in Beijing by synoptic weather pattern in planetary boundary layer. J. Geophys. Res. Atmos. 127, e2021JD035988.
Yang, Q., Xu, Y., Tong, X., Hu, T., Liu, Y., Chakraborty, T., Yao, R., Xiao, C., Chen, S., Ma, Z., 2023a. Influence of urban extent discrepancy on the estimation of surface urban heat island intensity: a global-scale assessment in 892 cities. J. Clean. Prod. 426, 139032.
Yang, Q., Xu, Y., Tong, X., Huang, X., Liu, Y., Chakraborty, T.C., Xiao, C., Hu, T., 2023b. An adaptive synchronous extraction (ASE) method for estimating intensity and footprint of surface urban heat islands: a case study of 254 north American cities. Remote Sens. Environ. 297, 113777.
Yang, Y., Guo, M., Wang, L., Zong, L., Liu, D., Zhang, W., Wang, M., Wan, B., Guo, Y., 2023c. Unevenly spatiotemporal distribution of urban excess warming in coastal Shanghai megacity, China: roles of geophysical environment, ventilation and sea breezes. Build. Environ. 235, 110180.
Yang, Q., Xu, Y., Wen, D., Hu, T., Chakraborty, T., Liu, Y., Yao, R., Chen, S., Xiao, C., Yang, J., 2024. Satellite clear-sky observations overestimate surface urban Heat Islands in humid cities. Geophys. Res. Lett. 51, e2023GL106995.
Yao, R., Wang, L., Huang, X., Niu, Z., Liu, F., Wang, Q., 2017. Temporal trends of surface urban heat islands and associated determinants in major Chinese cities. Sci. Total Environ. 609, 742–754.
Yao, R., Wang, L., Huang, X., Chen, J., Li, J., Niu, Z., 2018a. Less sensitive of urban surface to climate variability than rural in northern China. Sci. Total Environ. 628, 650–660.
Yao, R., Wang, L., Huang, X., Niu, Y., Chen, Y., Niu, Z., 2018b. The influence of different data and method on estimating the surface urban heat island intensity. Ecol. Indic. 89, 45–55.
Yao, R., Wang, L., Huang, X., Gong, W., Xia, X., 2019. Greening in rural areas increases the surface urban heat island intensity. Geophys. Res. Lett. 46, 2204–2212.
Yao, R., Wang, L., Huang, X., Cao, Q., Wei, J., He, P., Wang, S., Wang, L., 2023. Global seamless and high-resolution temperature dataset (GSHTD), 2001–2020. Remote Sens. Environ. 286, 113422.
Yu, P., Zhao, T., Shi, J., Ran, Y., Jia, L., Ji, D., Xue, H., 2022. Global spatiotemporally continuous MODIS land surface temperature dataset. Sci. Data 9, 143.
Yuan, B., Li, X., Zhou, L., Bai, T., Hu, T., Huang, J., Liu, D., Li, Y., Guo, J., 2023. Global distinct variations of surface urban heat islands in inter-and intra-cities revealed by local climate zones and seamless daily land surface temperature data. ISPRS J. Photogramm. Remote Sens. 204, 1–14.
Zhang, T., Zhou, Y., Zhao, K., Zhu, Z., Chen, G., Hu, J., Wang, L., 2022a. A global dataset of daily maximum and minimum near-surface air temperature at 1 km resolution over land (2003–2020). Earth Syst. Sci. Data 14, 5637–5649.
Zhang, T., Zhou, Y., Zhu, Z., Li, X., Asrar, G.R., 2022b. A global seamless 1 km resolution daily land surface temperature dataset (2003–2020). Earth Syst. Sci. Data 14, 651–664.
Zhang, H., Luo, M., Zhao, Y., Lin, L., Ge, E., Yang, Y., Ning, G., Cong, J., Zeng, Z., Gui, K., 2023. HiTIC-monthly: a monthly high spatial resolution (1 km) human thermal index collection over China during 2003–2020. Earth Syst. Sci. Data 15, 359–381.
Zhang, L., Luo, F., Pan, G., Zhang, W., Ren, G., Zheng, Z., Yang, Y., 2024. Elucidating the multi-timescale variability of a canopy urban Heat Island by using the short-time Fourier transform. Geophys. Res. Lett. 51, e2023GL106221.
Zhao, L., Lee, X., Smith, R.B., Oleson, K., 2014. Strong contributions of local background climate to urban heat islands. Nature 511, 216–219.
Zhao, M., Zhou, Y., Li, X., Cao, W., He, C., Yu, B., Li, X., Elvidge, C.D., Cheng, W., Zhou, C., 2019. Applications of satellite remote sensing of nighttime light observations: advances, challenges, and perspectives. Remote Sens. 11, 1971.
Zhao, N., Cao, G., Zhang, W., Samson, E.L., Chen, Y., 2020. Remote sensing and social sensing for socioeconomic systems: a comparison study between nighttime lights and location-based social media at the 500 m spatial resolution. Int. J. Appl. Earth Obs. Geoinf. 87, 102058.
Zhao, M., Cheng, C., Zhou, Y., Li, X., Shen, S., Song, C., 2022. A global dataset of annual urban extents (1992–2020) from harmonized nighttime lights. Earth Syst. Sci. Data 14, 517–534.
Zheng, Q., Weng, Q., Wang, K., 2019. Developing a new cross-sensor calibration model for DMSP-OLS and Suomi-NPP VIIRS night-light imageries. ISPRS J. Photogramm. Remote Sens. 153, 36–47.
Zhou, D., Zhao, S., Liu, S., Zhang, L., Zhu, C., 2014. Surface urban heat island in China's 32 major cities: spatial patterns and drivers. Remote Sens. Environ. 152, 51–61.
Zhou, D., Zhao, S., Zhang, L., Sun, G., Liu, Y., 2015. The footprint of urban heat island effect in China. Sci. Rep. 5, 11160.
Zhou, D., Zhang, L., Hao, L., Sun, G., Liu, Y., Zhu, C., 2016. Spatiotemporal trends of urban heat island effect along the urban development intensity gradient in China. Sci. Total Environ. 544, 617–626.
Zhou, B., Rybski, D., Kropp, J.P., 2017. The role of city size and urban form in the surface urban heat island. Sci. Rep. 7, 4791.
Zhou, D., Xiao, J., Bonafoni, S., Berger, C., Deilami, K., Zhou, Y., Frolking, S., Yao, R., Qiao, Z., Sobrino, J.A., 2018. Satellite remote sensing of surface urban heat islands: progress, challenges, and perspectives. Remote Sens. 11, 48.